Computational and Applied Mathematics Journal
2015; 1(5): 319-343
Published online July 10, 2015 (http://www.aascit.org/journal/camj)

AASCIT American Association for Science and Technology

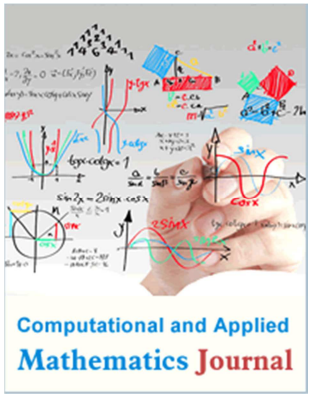

Keywords
Sparlat and Allmaras Model,
Menter and Rumsey Model,
Gibson and Dafa'Alla Model,
Navier-Stokes Equations,
Three-Dimensions

Received: June 15, 2015
Revised: June 26, 2015
Accepted: June 27, 2015

Assessment of Several Turbulence Models Applied to Supersonic Flows in Three-Dimensions – Part III

Edisson S. G. Maciel

Aeronautical Engineering Division (IEA), Aeronautical Technological Institute (ITA), São José dos Campos, São Paulo, Brazil

Email address
edisavio@edissonsavio.eng.br

Citation
Edisson S. G. Maciel. Assessment of Several Turbulence Models Applied to Supersonic Flows in Three-Dimensions – Part III. *Computational and Applied Mathematics Journal.* Vol. 1, No. 5, 2015, pp. 319-343.

Abstract
In the present work, the Van Leer and the Liou and Steffen Jr. flux vector splitting schemes are implemented to solve the three-dimensional Favre-averaged Navier-Stokes equations. The Sparlat and Allmaras one-equation model, and the Menter and Rumsey and the Gibson and Dafa'Alla two-equation models are used in order to close the problem. The physical problem under study is the supersonic flow around a blunt body. The results have demonstrated that the Van Leer scheme using the Menter and Rumsey turbulence model in its SST variant has yielded the best value of the stagnation pressure and is the most efficient scheme.

1. Introduction

Conventional non-upwind algorithms have been used extensively to solve a wide variety of problems ([1]). Conventional algorithms are somewhat unreliable in the sense that for every different problem (and sometimes, every different case in the same class of problems) artificial dissipation terms must be specially tuned and judicially chosen for convergence. Also, complex problems with shocks and steep compression and expansion gradients may defy solution altogether.

Upwind schemes are in general more robust but are also more involved in their derivation and application. Some upwind schemes that have been applied to the Euler equations are: [2-3]. A description of these methods is found in [4].

In relation to turbulent flow simulations, [5] applied the Navier-Stokes equations to transonic flows problems along a convergent-divergent nozzle and around the NACA 0012 airfoil. The [6] model was used to close the problem. Three algorithms were implemented: the [7] explicit scheme, the [8] implicit scheme and the [9] explicit scheme. The results have shown that, in general terms, the [7] and the [9] schemes have presented better solutions.

For a more detailed description of the motivation of the present study, as well some comments about different turbulence models the reader is encouraged to read [4].

In the present work, the [2-3] flux vector splittin g schemes are implemented, on a finite-volume context. The three-dimensional Favre-averaged Navier-Stokes equations are solved using an upwind discretization on a structured mesh. The [10] one-equation model, and the [11] and [12] k-ω and $k^{1/2}$-ζ two-equation models, respectively, are used in order to close the problem. The physical problem under study is the supersonic flow around a blunt body configuration. The implemented schemes are first-order accurate in space. The time integration uses a Runge-Kutta method of five stages and is second-order accurate. The algorithms are accelerated to the steady state solution using a spatially

variable time step. This technique has proved excellent gains in terms of convergence rate as reported in [13-14]. The results have demonstrated that the [2] scheme using the [11] turbulence model in its SST variant has yielded the best value of thestagnation pressure and is the most efficient computational scheme.

2. Three-Dimensional Navier-Stokes Equations

The three-dimensional flow is modeled by the Navier-Stokes equations, which express the conservation of mass and energy as well as the momentum variation of a viscous, heat conducting and compressible media, in the absence of external forces. The Navier-Stokes equations are presented in their two-equation turbulence model formulation. The one-equation model considers only one additional equation that is solved in place of the two-equation formulation. The integral form of these equations may be represented by:

$$\partial/\partial t\int_V Q dV+\int_S\left[\left(E_e-E_v\right)n_x+\left(F_e-F_v\right)n_y+\left(G_e-G_v\right)n_z\right]dS+\int_V M dV=0\,, \tag{1}$$

where Q is written for a Cartesian system, V is the cell volume, n_x, n_y, and n_z are components of the unity vector normal to the cell boundary, S is the flux area, E_e, F_e and G_e are the components of the convective, or Euler, flux vector, E_v, F_v and G_v are the components of the viscous, or diffusive, flux vector and M is the source term of the two-equation models. The vectors Q, E_e, F_e, G_e, E_v, F_v, G_v, and M are, incorporating a k-s formulation, represented by:

$$Q=\begin{Bmatrix}\rho\\ \rho u\\ \rho v\\ \rho w\\ e\\ \rho k\\ \rho s\end{Bmatrix},\ E_e=\begin{Bmatrix}\rho u\\ \rho u^2+p\\ \rho uv\\ \rho uw\\ (e+p)u\\ \rho ku\\ \rho su\end{Bmatrix},\ F_e=\begin{Bmatrix}\rho v\\ \rho vu\\ \rho v^2+p\\ \rho vw\\ (e+p)v\\ \rho kv\\ \rho sv\end{Bmatrix},\ G_e=\begin{Bmatrix}\rho w\\ \rho wu\\ \rho wv\\ \rho w^2+p\\ (e+p)w\\ \rho kw\\ \rho sw\end{Bmatrix};\tag{2}$$

$$E_v=\begin{Bmatrix}0\\ t_{xx}+\tau_{xx}\\ t_{xy}+\tau_{xy}\\ t_{xz}+\tau_{xz}\\ f_x\\ \alpha_x\\ \beta_x\end{Bmatrix},\ F_v=\begin{Bmatrix}0\\ t_{xy}+\tau_{xy}\\ t_{yy}+\tau_{yy}\\ t_{yz}+\tau_{yz}\\ f_y\\ \alpha_y\\ \beta_y\end{Bmatrix},\ G_v=\begin{Bmatrix}0\\ t_{xz}+\tau_{xz}\\ t_{yz}+\tau_{yz}\\ t_{zz}+\tau_{zz}\\ f_z\\ \alpha_z\\ \beta_z\end{Bmatrix};\tag{3}$$

$$M=\{0\quad 0\quad 0\quad 0\quad 0\quad M_k\quad M_s\}^T,\tag{4}$$

where the components of the viscous stress tensor are defined as:

$$\begin{aligned}
t_{xx}&=\left[2\mu_M\,\partial u/\partial x-2/3\mu_M\left(\partial u/\partial x+\partial v/\partial y+\partial w/\partial z\right)\right]/\mathrm{Re};\\
t_{xy}&=\mu_M\left(\partial u/\partial y+\partial v/\partial x\right)/\mathrm{Re};\\
t_{xz}&=\mu_M\left(\partial u/\partial z+\partial w/\partial x\right)/\mathrm{Re};\\
t_{yy}&=\left[2\mu_M\left(\partial v/\partial y\right)-2/3\mu_M\left(\partial u/\partial x+\partial v/\partial y+\partial w/\partial z\right)\right]/\mathrm{Re};\\
t_{yz}&=\mu_M\left(\partial v/\partial z+\partial w/\partial y\right)/\mathrm{Re};\\
t_{zz}&=\left[2\mu_M\left(\partial w/\partial z\right)-2/3\mu_M\left(\partial u/\partial x+\partial v/\partial y+\partial w/\partial z\right)\right]/\mathrm{Re}.
\end{aligned}\tag{5}$$

The components of the turbulent stress tensor (Reynolds stress tensor) are described by the following expressions:

$$\begin{aligned}
\tau_{xx}&=\left[2\mu_T\,\partial u/\partial x-2/3\mu_T\left(\partial u/\partial x+\partial v/\partial y+\partial w/\partial z\right)\right]/\mathrm{Re}\ -2/3\rho k;\\
\tau_{xy}&=\mu_T\left(\partial u/\partial y+\partial v/\partial x\right)/\mathrm{Re};\\
\tau_{xz}&=\mu_T\left(\partial u/\partial z+\partial w/\partial x\right)/\mathrm{Re};\\
\tau_{yy}&=\left[2\mu_T\left(\partial v/\partial y\right)-2/3\mu_T\left(\partial u/\partial x+\partial v/\partial y+\partial w/\partial z\right)\right]/\mathrm{Re}-2/3\rho k;\\
\tau_{yz}&=\mu_T\left(\partial v/\partial z+\partial w/\partial y\right)/\mathrm{Re};\\
\tau_{zz}&=\left[2\mu_T\left(\partial w/\partial z\right)-2/3\mu_T\left(\partial u/\partial x+\partial v/\partial y+\partial w/\partial z\right)\right]/\mathrm{Re}-2/3\rho k.
\end{aligned}\tag{6}$$

Expressions to f_x, f_y and f_z are given below:

$$\begin{aligned}
f_x&=\left(t_{xx}+\tau_{xx}\right)u+\left(t_{xy}+\tau_{xy}\right)v+\left(t_{xz}+\tau_{xz}\right)w-q_x\\
f_y&=\left(t_{xy}+\tau_{xy}\right)u+\left(t_{yy}+\tau_{yy}\right)v+\left(t_{yz}+\tau_{yz}\right)w-q_y\,,\\
f_z&=\left(t_{xz}+\tau_{xz}\right)u+\left(t_{yz}+\tau_{yz}\right)v+\left(t_{zz}+\tau_{zz}\right)w-q_z
\end{aligned}\tag{7}$$

where q_x, q_y and q_z are the Fourier heat flux components and are given by:

$$\begin{aligned}
q_x&=-\gamma/\mathrm{Re}\left(\mu_M/\mathrm{Pr}_L+\mu_T/\mathrm{Pr}_T\right)\partial e_i/\partial x;\\
q_y&=-\gamma/\mathrm{Re}\left(\mu_M/\mathrm{Pr}_L+\mu_T/\mathrm{Pr}_T\right)\partial e_i/\partial y;\\
q_z&=-\gamma/\mathrm{Re}\left(\mu_M/\mathrm{Pr}_L+\mu_T/\mathrm{Pr}_T\right)\partial e_i/\partial z.
\end{aligned}\tag{8}$$

The diffusion terms related to the k-s equations are defined as:

$$\begin{aligned}
\alpha_x&=1/\mathrm{Re}\left(\mu_M+\mu_T/\sigma_k\right)\partial k/\partial x;\\
\alpha_y&=1/\mathrm{Re}\left(\mu_M+\mu_T/\sigma_k\right)\partial k/\partial y;\\
\alpha_z&=1/\mathrm{Re}\left(\mu_M+\mu_T/\sigma_k\right)\partial k/\partial z;
\end{aligned}\tag{9}$$

$$\begin{aligned}
\beta_x&=1/\mathrm{Re}\left(\mu_M+\mu_T/\sigma_s\right)\partial s/\partial x;\\
\beta_y&=1/\mathrm{Re}\left(\mu_M+\mu_T/\sigma_s\right)\partial s/\partial y;\\
\beta_z&=1/\mathrm{Re}\left(\mu_M+\mu_T/\sigma_s\right)\partial s/\partial z.
\end{aligned}\tag{10}$$

In the above equations, ρ is the fluid density; u, v and w are Cartesian components of the velocity vector in the x, y and z directions, respectively; e is the total energy per unit volume;

p is the static pressure; k is the turbulence kinetic energy; s is the second turbulent variable, which is the vorticity (k-ω model) or the rate of dissipation ($k^{1/2}$-ζ model) for this work; the t's are viscous stress components; τ's are the Reynolds stress components; the q's are the Fourier heat flux components; M_k takes into account the production and the dissipation terms of k; M_s takes into account the production and the dissipation terms of s; μ_M and μ_T are the molecular and the turbulent viscosities, respectively; Pr_L and Pr_T are the laminar and the turbulent Prandtl numbers, respectively; σ_k and σ_s are turbulence coefficients; γ is the ratio of specific heats; Re is the viscous Reynolds number, defined by:

$$Re = \rho V_{REF} l_{REF} / \mu_M \ , \tag{11}$$

where V_{REF} is a characteristic flow velocity and l_{REF} is a configuration characteristic length. The internal energy of the fluid, e_i, is defined as:

$$e_i = e/\rho - 0.5\left(u^2 + v^2 + w^2\right). \tag{12}$$

The molecular viscosity is estimated by the empiric Sutherland formula:

$$\mu_M = bT^{1/2} / \left(1 + S/T\right), \tag{13}$$

where T is the absolute temperature (K), b = 1.458×10^{-6} Kg/(m.s.$K^{1/2}$) and S = 110.4 K, to the atmospheric air in the standard atmospheric conditions ([15]).

The Navier-Stokes equations are dimensionless in relation to the freestream density, ρ_∞, the freestream speed of sound, a_∞, and the freestream molecular viscosity, μ_∞. The system is closed by the state equation for a perfect gas:

$$p = (\gamma - 1)\left[e - 0.5\rho\left(u^2 + v^2 + w^2\right) - \rho k\right], \tag{14}$$

considering the ideal gas hypothesis. The total enthalpy is given by $H = \left(e + p\right)/\rho$.

The [2-3] flux vector splitting algorithms are described in detail in [4] and the interested reader is encouraged to read this work. The viscous implementation is also described in [4]. The three-dimensional configuration like: computational cell, flux surface areas, normal vectors and cell volume are described in [16]. The spatially variable time step is described in [4; 17] and the interested reader can found in these references the detailed implementation.

3. Turbulence Models

3.1. Sparlat and Allmaras Turbulence Model

The purpose of the [10] one-equation model was overcome the algebraic model limitations and, at the same time, to avoid the difficulties in the implementation of the two-equation models or the Reynolds stress equations. This model employs a transport turbulent viscosity to solve the turbulence scaling. Such model takes naturally into account the turbulence and diffusion histories, which improves its accuracy.

The transport equation to the work turbulent kinematic viscosity is described by:

$$\frac{D\tilde{\nu}}{Dt} = c_{b1}\tilde{S}\tilde{\nu} + \frac{1}{\sigma}\left[\nabla \bullet \left((\nu + \tilde{\nu})\nabla\tilde{\nu}\right) + c_{b2}\left(\nabla\tilde{\nu}\right)^2\right] - c_{w1} f_w(r)\left(\frac{\tilde{\nu}}{N}\right)^2. \tag{15}$$

In this equation, the first term of the right-hand-side is the production contribution to the work kinematic viscosity; the second term is the viscosity diffusion; and the last term is the destruction of the work kinematic viscosity. The turbulent viscosity is defined by:

$$\mu_T = \rho\tilde{\nu} f_{v1}. \tag{16}$$

With the purpose of assuring that $\tilde{\nu}$ becomes equal to $K \times N \times \sqrt{\tau_{xy,w}/\rho_w}$ in the logarithmic layer and in the viscous sub-layer, the f_{v1} damping function is defined by:

$$f_{v1} = \frac{\lambda^3}{\lambda^3 + {c_{v1}}^3} \tag{17}$$

as function of the $\lambda = \tilde{\nu}/\nu$ variable. The $\tilde{S}$ function, representing the deformation work of the mean flow, is determined as follows:

$$\tilde{S} = \sqrt{\left(\frac{\partial v}{\partial z} - \frac{\partial w}{\partial y}\right)^2 + \left(\frac{\partial w}{\partial x} - \frac{\partial u}{\partial z}\right)^2 + \left(\frac{\partial u}{\partial y} - \frac{\partial v}{\partial x}\right)^2} + \left[\frac{\tilde{\nu}}{(\kappa N)^2} f_{v2}\right], \tag{18}$$

in which f_{v2} has the following expression:

$$f_{v2} = 1 - \frac{\lambda}{1 + \lambda f_{v1}}. \tag{19}$$

The destruction term should disappear at the external region of the boundary layer. [17] purposes the following function to reproduce such behavior:

$$f_w(r) = g\left[\frac{1 + {c_{w3}}^6}{g^6 + {c_{w3}}^6}\right]^{1/6}, \quad g = r + c_{w2}\left(r^6 - r\right), \quad r = \frac{\tilde{\nu}}{(\kappa N)^2 \tilde{S}}, \tag{20}$$

where r is the argument and f_w is a function reaching the value 1.0 at the logarithmic layer and decreasing at the external region. The g function is merely a limiter to prevent f_w high values. The [10] model constants are:

$$c_{b1} = 0{,}1355, \ c_{b2} = 0{,}622, \ c_{w2} = 0{,}3, \ c_{v1} = 7{,}1,$$

$$\sigma = 2/3, \ c_{w3} = 2{,}0, \ c_{w1} = \frac{c_{b1}}{\kappa^2} + \frac{\left(1 + c_{b2}\right)}{\sigma}. \tag{21}$$

The [10] model is marched in time using a LU-SGS ("Lower-Upper Factorization – Symmetrical Gauss-Seidel") implicit method. Details of the implicit implementation in two-dimensions are found in [10]. The extension to three-dimensions is straightforward.

In this work, the term referent to the diffusion of the work kinematic viscosity was not implemented. The studied model considers only the production and dissipation terms of the work kinematic viscosity.

3.2. Menter and Rumsey Turbulence Model

The [11] model presents four variants: k-ω model of Wilcox, k-ε of two layers, BSL model of [18], and SST (Shear Stress Transport) model of [18]. They are defined as follows:

k-ω model of Wilcox. Constants of the k-ω model of [19]:

$$\beta_1^* = 0.09,\ \sigma_1^* = 0.5,\ \kappa_1 = 0.41,\ \gamma_1 = 5/9,\ \sigma_1 = 0.5 \text{ and } \beta_1 = \left(\gamma_1 + \sigma_1\kappa_1^2/\sqrt{\beta_1^*}\right)\beta_1^*;$$

Constants of the standard k-ε model of [20]:

$$C_\mu = 0.09,\ C_{\varepsilon 1} = 1.44,\ C_{\varepsilon 2} = 1.92,\ \sigma_k = 1.0, \text{ and } \sigma_\varepsilon = 1.17;$$

Constants of the equivalent k-ε model:

$$\beta_2^* = C_\mu,\ \sigma_2^* = 1/\sigma_k,\ \kappa_2 = 0.41,\ \gamma 2 = C_{\varepsilon 1} - 1.0,\ \sigma_2 = 1/\sigma_\varepsilon, \text{ and } \beta_2 = (C_{\varepsilon 2} - 1.0)C_\mu;$$

Weighting function, F_1:
$F_1 = 1.0$;
Turbulent viscosity:

$$\mu_T = \mathrm{Re}\rho k/\omega; \tag{22}$$

k-ε model of two layers. Constants of the k-ω model of [19]:

$$\beta_1^* = 0.09,\ \sigma_1^* = 0.5,\ \kappa_1 = 0.41,\ \gamma_1 = 5/9,\ \sigma_1 = 0.4 \text{ and } \beta_1 = \left(\gamma_1 + \sigma_1\kappa_1^2/\sqrt{\beta_1^*}\right)\beta_1^*;$$

Constants of the equivalent k-ε model:

$$\beta_2^* = 0.09,\ \sigma_2^* = 1.0,\ \kappa_2 = 0.41,\ \gamma_2 = 0.44,\ \sigma_2 = 0.857, \text{ and } \beta_2 = \left(\gamma_2 + \sigma_2\kappa_2^2/\sqrt{\beta_2^*}\right)\beta_2^*;$$

Weighting function, F_1:
Γ_1 parameter:

$$\Gamma_1 = 500\upsilon_M/\left(n^2\omega\right), \tag{23}$$

with: $\upsilon_M = \mu_M/\rho$ and n = normal distance from the wall to the cell under study;
Coefficient CDk-ω:

$$CD_{k-\omega} = MAX\left[\left(2\rho\sigma_2/\omega\frac{\partial k}{\partial y}\frac{\partial \omega}{\partial y}\right)\Big/\mathrm{Re},\ 10^{-20}\right]; \tag{24}$$

Γ_2 parameter:

$$\Gamma_2 = 4\rho\sigma_2 k/\left(n^2 CD_{k-\omega}\right) \tag{25}$$

Γ_M parameter:

$$\Gamma_M = MIN(\Gamma_1, \Gamma_2); \tag{26}$$

$$F_1 = TANH\left(\Gamma_M^4\right); \tag{27}$$

Turbulent viscosity:

$$\mu_T = \mathrm{Re}\rho k/\omega; \tag{28}$$

Menter's BSL model. Constants of the k-ω model of [19]:

$$\beta_1^* = 0.09,\ \sigma_1^* = 0.5,\ \kappa_1 = 0.41,\ \gamma_1 = 5/9,\ \sigma_1 = 0.5 \text{ and } \beta_1 = \left(\gamma_1 + \sigma_1\kappa_1^2/\sqrt{\beta_1^*}\right)\beta_1^*;$$

Constants of the equivalent k-ε model:

$$\beta_2^* = 0.09,\ \sigma_2^* = 1.0,\ \kappa_2 = 0.41,\ \gamma_2 = 0.44,\ \sigma_2 = 0.857, \text{ and } \beta_2 = \left(\gamma_2 + \sigma_2\kappa_2^2/\sqrt{\beta_2^*}\right)\beta_2^*;$$

Weighting function, F_1:
Γ_1 parameter:

$$\Gamma_1 = 500\upsilon_M/\left(n^2\omega\right);$$

Coefficient $CD_{k\text{-}\omega}$:

$$CD_{k-\omega} = MAX\left[\left(2\rho\sigma_2/\omega\frac{\partial k}{\partial y}\frac{\partial \omega}{\partial y}\right)\Big/\mathrm{Re},\ 10^{-20}\right];$$

Γ_2 parameter:

$$\Gamma_2 = 4\rho\sigma_2 k/\left(n^2 CD_{k-\omega}\right);$$

Γ_3 parameter:

$$\Gamma_3 = \sqrt{k}/\left(\beta_1^* \omega n\right); \quad (29)$$

Γ_M parameter:

$$\Gamma_M = \text{MIN}[\text{MAX}(\Gamma_1, \Gamma_3), \Gamma_2]; \quad (30)$$

$$F_1 = \text{TANH}\left(\Gamma_M^4\right);$$

Turbulent viscosity:

$$\mu_T = \text{Re}\,\rho k / \omega; \quad (31)$$

Menter's SST model. Constants of the k-ω model of [19]:

$\beta_1^* = 0.09$, $\sigma_1^* = 0.5$, $\kappa_1 = 0.41$, $\gamma_1 = 5/9$, $\sigma_1 = 0.5$ and

$$\beta_1 = \left(\gamma_1 + \sigma_1 \kappa_1^2 / \sqrt{\beta_1^*}\right)\beta_1^*;$$

Constants of the equivalent k-ε model:

$\beta_2^* = 0.09$, $\sigma_2^* = 1.0$, $\kappa_2 = 0.41$, $\gamma 2 = 0.44$, $\sigma_2 = 0.857$,

and $\beta_2 = \left(\gamma_2 + \sigma_2 \kappa_2^2 / \sqrt{\beta_2^*}\right)\beta_2^*$;

Weighting function, F_1:

Γ_1 parameter:

$$\Gamma_1 = 500\upsilon_M / \left(n^2 \omega\right);$$

Coefficient $CD_{k\text{-}\omega}$:

$$CD_{k-\omega} = \text{MAX}\left[\left(2\rho\sigma_2 / \omega \frac{\partial k}{\partial y}\frac{\partial \omega}{\partial y}\right)\Big/ \text{Re},\ 10^{-20}\right];$$

Γ_2 parameter:

$$\Gamma_2 = 4\rho\sigma_2 k / \left(n^2 CD_{k-\omega}\right);$$

Γ_3 parameter:

$$\Gamma_3 = \sqrt{k}/\left(\beta_1^* \omega n\right);$$

Γ_M parameter:

$$\Gamma_M = \text{MIN}[\text{MAX}(\Gamma_1, \Gamma_3), \Gamma_2];$$

$$F_1 = \text{TANH}\left(\Gamma_M^4\right);$$

Weighting function, F_2:

Γ_M parameter:

$$\Gamma_M = \text{MIN}(2\Gamma_3, \Gamma_1); \quad (32)$$

$$F_2 = \text{TANH}\left(\Gamma_M^2\right); \quad (33)$$

$$\Omega = |\partial u/\partial y| + |\partial v/\partial z| + |\partial w/\partial x|; \quad (34)$$

Turbulent viscosity:

$$\mu_T = \rho \text{MIN}[k/\omega, a_1 k/(\Omega F_2)]\text{Re}, \quad (35)$$

where $a_1 = 0.31$.

With these definitions, each model can determine the following additional constants:

$$\sigma^* = \sigma_1^* F_1 + (1 - F_1)\sigma_2^*; \quad (36)$$

$$\sigma = \sigma_1 F_1 + (1 - F_1)\sigma_2; \quad (37)$$

$$\sigma_k = 1/\sigma^* \quad \text{and} \quad \sigma_\omega = 1/\sigma; \quad (38)$$

$$\gamma = \gamma_1 F_1 + (1 - F_1)\gamma_2; \quad (39)$$

$$\beta = \beta_1 F_1 + (1 - F_1)\beta_2; \quad (40)$$

$$\beta^* = \beta_1^* F_1 + (1 - F_1)\beta_2^*. \quad (41)$$

The source term denoted by G in the governing equations contains the production and dissipation terms of k and ω. To the [11] model, the G_k and G_ω terms have the following expressions:

$$G_k = -P_k + D_k \quad \text{and} \quad G_\omega = -P_\omega + D_\omega - Dif_\omega, \quad (42)$$

where:

$$P_k = \mu_T\left(\frac{\partial u}{\partial y} + \frac{\partial v}{\partial x}\right)\frac{\partial u}{\partial y}\Big/\text{Re} + \mu_T\left(\frac{\partial u}{\partial z} + \frac{\partial w}{\partial x}\right)\frac{\partial w}{\partial x}\Big/\text{Re} + \mu_T\left(\frac{\partial v}{\partial z} + \frac{\partial w}{\partial y}\right)\frac{\partial v}{\partial z}\Big/\text{Re}; \quad (43)$$

$$D_k = \beta^* \rho k \omega / \text{Re}; \quad (44)$$

$$P_\omega = \gamma P_k / \upsilon_T; \quad D_\omega = \beta\rho\omega^2 / \text{Re}; \quad (45)$$

$$Dif_\omega = (1 - F_1)\frac{2\rho\sigma_2}{\omega}\frac{\partial k}{\partial y}\frac{\partial \omega}{\partial y}\Big/\text{Re}, \quad (46)$$

with: $\upsilon_T = \mu_T / \rho$.

3.3. Gibson and Dafa'Alla Turbulence Model

In the [12] turbulence model, k is replaced by q and s = ζ, where the equivalence between k and q is $k = q^2$. This model has two variants based on the works of [20] and [21]. Initially, it is necessary to calculate the turbulent Reynolds number

$$R_t = k^2 / \left(\upsilon_m^2 \zeta\right). \quad (47)$$

The function f_μ is estimated by [20-21] as

$$f_\mu = \begin{cases} e^{\left[\frac{-6}{(1+R_t/50)^2}\right]}, & [20]; \\ 1 - e^{\left(-0.0115N^+\right)}, & [21], \end{cases} \quad (48)$$

where $N^+ = \sqrt{Re}\sqrt{\frac{\tau_{xy,w}}{\rho_w}}\frac{N}{\upsilon_{M,w}}$ and N is the normal distance from the surface to the cell under study.

The turbulent viscosity is expressed in terms of q and ζ as:

$$\mu_T = Re\, C_\mu \rho f_\mu q^3 / 2\zeta . \quad (49)$$

To the [12] model, the G_q and G_ζ terms have the following expressions:

$$G_q = -P_q + D_q \quad \text{and} \quad G_\zeta = -P_\zeta + D_\zeta , \quad (50)$$

where:

$$P_q = \rho\gamma_T \left[\left(\frac{\partial u}{\partial y}+\frac{\partial v}{\partial x}\right)\frac{\partial u}{\partial y}+\left(\frac{\partial u}{\partial z}+\frac{\partial w}{\partial x}\right)\frac{\partial w}{\partial x}+\left(\frac{\partial v}{\partial z}+\frac{\partial w}{\partial y}\right)\frac{\partial v}{\partial z}\right] \Big/ Re ; \quad (51)$$

$$D_k = \rho\zeta / Re ; \quad (52)$$

$$P_\zeta = \left(\frac{\zeta}{q}\right) C_{z1} f_{z1} P_k \quad \text{and} \quad D_\zeta = \rho\left(\frac{\zeta^2}{q} C_{z2} f_{z2} - \xi_1\right) \Big/ Re , \quad (53)$$

where:

$$f_{e2} = \begin{cases} 1-0.3e^{-R_t^2}, & [20]; \\ 1-0.22e^{-R_t^2/36}, & [21]; \end{cases} \quad (54)$$

$$\gamma_t = 0.25 C_\mu f_\mu \, q^2 / \zeta ; \quad (55)$$

$$C_{z1} f_{z1} = 2C_{e1} f_{e1} - 1 ; \; C_{z2} f_{z2} = 2C_{e2} f_{e2} - 1 ; \quad (56)$$

$$\xi_1 = -2\upsilon_m \left(\zeta / N^2\right) e^{-0.5N^+} . \quad (57)$$

where the closure coefficients adopted for the [12] model are defined in Tab. 1.

Table 1. *Closure coefficients.*

Constant	[20]	[21]
σ_q	1.0	1.0
σ_ζ	1.3	1.3
C_μ	0.09	0.09
C_{e1}	1.44	1.35
C_{e2}	1.92	1.80
f_{e1}	1.0	1.0

4. Initial and Boundary Conditions

The initial and boundary conditions to the [10] turbulence model are the same of those found in [22-23]. To the [11] turbulence model are the same of those found in [4; 24]. For the $k^{1/2}$-ζ, one has:

4.1. Initial Condition

Freestream values, at all grid cells, are adopted for all flow properties as initial condition, as suggested by [25-26]. Therefore, the vector of conserved variables is defined as:

$$Q_{i,j,k} = \left\{1 \quad M_\infty \cos\alpha \quad M_\infty \sin\alpha\cos\theta \quad M_\infty \sin\alpha\sin\theta \quad \frac{1}{\gamma(\gamma-1)} + 0.5M_\infty^2 \quad k_\infty^{1/2} \quad \zeta_\infty\right\}^T , \quad (58)$$

where k_∞ is the freestream turbulent kinetic energy and ζ_∞ is the freestream turbulent dissipation rate. These parameters assume the following values: $k_\infty^{1/2} = 0.05M_\infty$ and $\zeta_\infty = M_\infty$.

4.2. Boundary Conditions

The boundary conditions are basically of four types: solid wall, entrance, exit and lateral planes. These conditions are implemented with the help of ghost cells.

(1) Wall condition: At a solid boundary the non-slip condition is enforced. Therefore, the tangent velocity component of the ghost volume at wall has the same magnitude as the respective velocity component of its real neighbor cell, but opposite signal. In the same way, the normal velocity component of the ghost volume at wall is equal in value, but opposite in signal, to the respective velocity component of its real neighbor cell.

The normal pressure gradient of the fluid at the wall is assumed to be equal to zero in a boundary-layer like condition. The same hypothesis is applied for the normal temperature gradient at the wall, assuming an adiabatic wall. The normal gradient of the turbulence kinetic energy at the wall is also assumed to be equal to zero.

From the above considerations, density and pressure are extrapolated from the respective values of its real neighbor volume (zero order extrapolation). The total energy is obtained by the state equation for a perfect gas. The turbulent kinetic energy at the ghost volume is extrapolated from the neighbor cell and the turbulent dissipation rate at the ghost volume is determined by the following expression:

$$\zeta_{ghost} = 0.5\rho_{ghost} C_\mu^{3/4} \left(\rho k^{1/2}\right)^2_{ghost} \Big/ \left(0.41 d_n\right), \quad (59)$$

where d_n is the distance of the first cell to the wall. The wall law is used to specify the u component of velocity. Details of the wall law are found in [4].

(2) Entrance condition:

(2.1) Subsonic flow: Six properties are specified and one extrapolated. This approach is based on information propagation analysis along characteristic directions in the calculation domain ([26]). In other words, for subsonic flow, six characteristic propagate information pointing into the computational domain. Thus six flow properties must be fixed at the inlet plane. Just one characteristic line allows information to travel upstream. So, one flow variable must be extrapolated from the grid interior to the inlet boundary. The pressure was the extrapolated variable from the real neighbor

volumes, for the studied problem. Density and velocity components adopted values of freestream flow. The squared root of the turbulence kinetic energy is fixed with the value $0.05u_{ghost}$ and the turbulent dissipation rate was fixed with the value: $\zeta_{ghost} = 0.05u_{ghost}^2 / (\rho k^{1/2})_{ghost}$. The total energy is determined by the state equation of a perfect gas.

(2.2) Supersonic flow: In this case no information travels upstream; therefore all variables are fixed with their of freestream values.

(3) Exit condition:

(3.1) Subsonic flow: Six characteristic propagate information outward the computational domain. Hence, the associated variables should be extrapolated from interior information. The characteristic direction associated to the "$(q_{normal}$-a)" velocity should be specified because it points inward to the computational domain ([26]). In this case, the ghost volume pressure is specified from its initial value. Density, velocity components, the turbulence kinetic energy, and the turbulent dissipation rate are extrapolated. The total energy is obtained from the state equation of a perfect gas.

(3.2) Supersonic flow: All variables are extrapolated from interior grid cells, as no flow information can make its way upstream. In other words, nothing can be fixed.

(4) Lateral plane conditions: The flow tangency condition is stipulated for these boundaries. An Euler boundary is set up.

5. Results

Tests were performed in an INTEL Core i7 processor of 2.10GHz and 8.0Gbytes of RAM microcomputer in a Windows 7.0 environment. Three orders of reduction of the maximum residual in the field were considered to obtain a converged solution. The residual was defined as the value of the discretized conservation equation. The entrance or attack angle was adopted equal to zero, as well the longitudinal angle. The ratio of specific heats, γ, assumed the value 1.4.

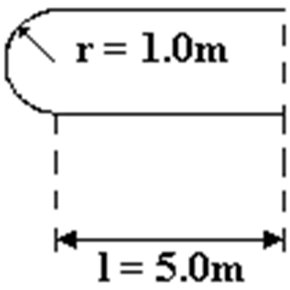

Figure 1. *Blunt body configuration.*

The initial data of the simulations is described in Tab. 2.

Table 2. *Initial Conditions.*

M_∞	α	θ	Altitude	L_∞	Re
3.0	0.0°	0.0°	40,000m	2.0m	$4.75x10^5$

Figure 1 shows the blunt body configuration, whereas Fig. 2 shows the blunt body mesh. A mesh of 53x50x10 points or composed of 22,932 hexahedron cells and 26,500 nodes was generated, employing an exponential stretching of 5.0% in the η direction.

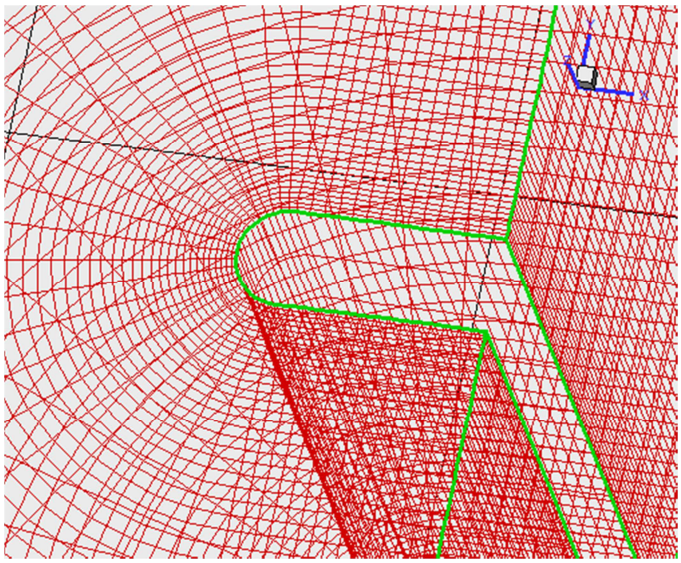

Figure 2. *Blunt body mesh.*

5.1. Sparlat and Allmaras Results

Figures 3 and 4 present the pressure contours obtained by the [2] and [3] schemes, respectively, as using the [10] turbulence model in three-dimensions. Both fields are homogeneous and the pressure contours generated by the [2] scheme is more strength than the respective one generated by the [3] scheme. Good symmetry properties are observed in both figures. The shock wave is well captured by both schemes as using the [10] turbulence model.

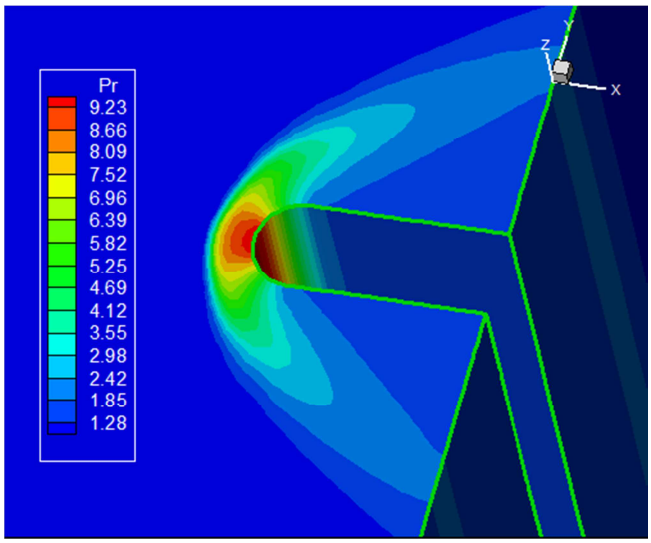

Figure 3. *Pressure contours ([2]).*

Figures 5 and 6 show the Mach number contours obtained by the [2] and [3] numerical schemes, respectively, as using the [10] turbulence model. Both Mach number fields are free of pre-shock oscillations and are homogeneous. The

differences between these fields are only in qualitative terms.

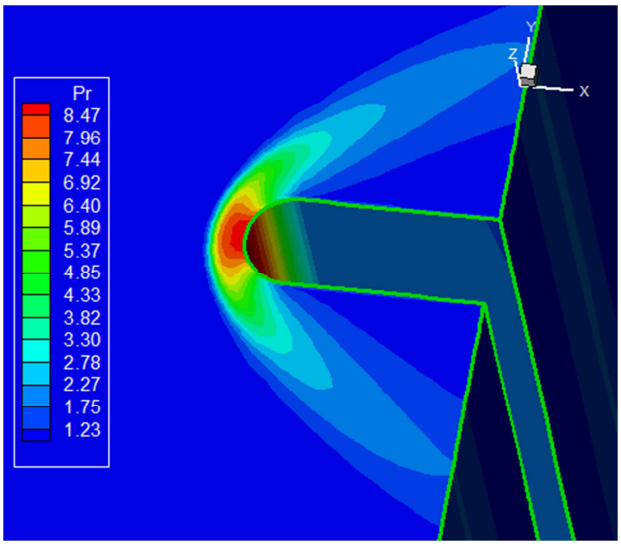

Figure 4. *Pressure contours ([3]).*

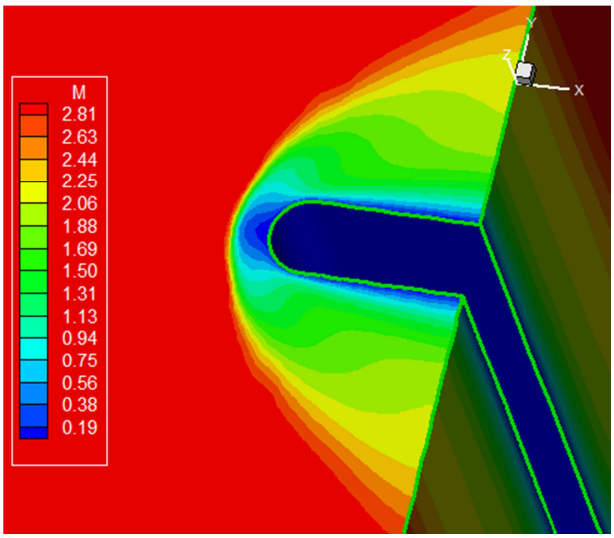

Figure 5. *Mach number contours ([2]).*

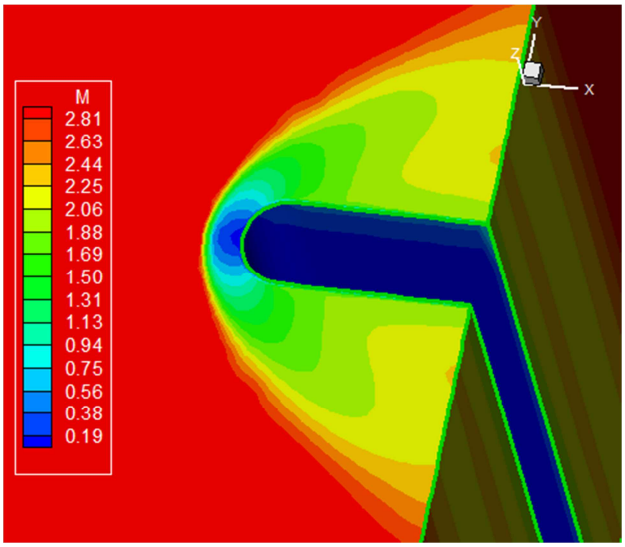

Figure 6. *Mach number contours ([3]).*

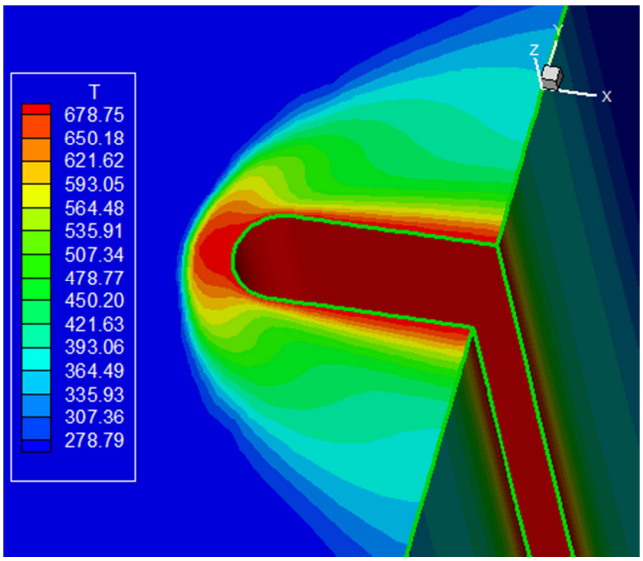

Figure 7. *Temperature contours ([2]).*

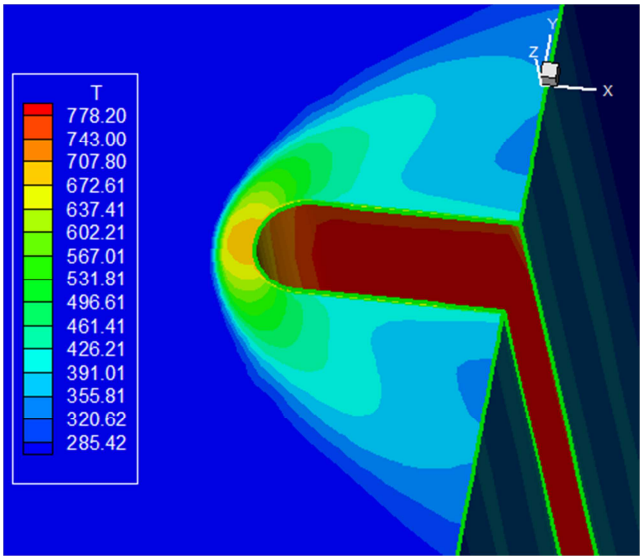

Figure 8. *Temperature contours ([3]).*

It is possible to see that the [2] solution develops a region of low Mach number contours close to the wall, resulting from the boundary layer formation.

Figures 7 and 8 exhibit the translational temperature contours obtained by the [2] and [3] schemes, respectively, as using the [10] turbulence model. The temperature contours generated by the [3] scheme is more intense than the respective one of the [2] scheme. However, the [2] solution presents a zone of high dissipation close to the wall, whereas the [3] scheme does not. There are qualitative differences between the two solutions, but both present homogeneous contours, without oscillations. Some problems with the [3] solution in the k = constant planes are observed, which prejudices the solution repetition in these planes. The [2] solution does not present such problems.

Figure 9 exhibits the -Cp distributions generated by the [2] and [3] schemes as using the [10] turbulence model. The -Cp plateau of the [2] scheme is higher than the -Cp plateau of the

[3] scheme. The -Cp peak at the body nose is the same for both schemes. Figure 10 presents the wall temperature distributions generated by the [2] and [3] numerical schemes as using the [10] turbulence model. The temperature distribution is smoother for the [2] scheme. The temperature distribution of the [3] scheme is more intense than the respective one of the [2] scheme. The maximum temperature obtained by the [2] scheme is about 708.0 K, whereas that obtained by the [3] scheme is about 814.0 K.

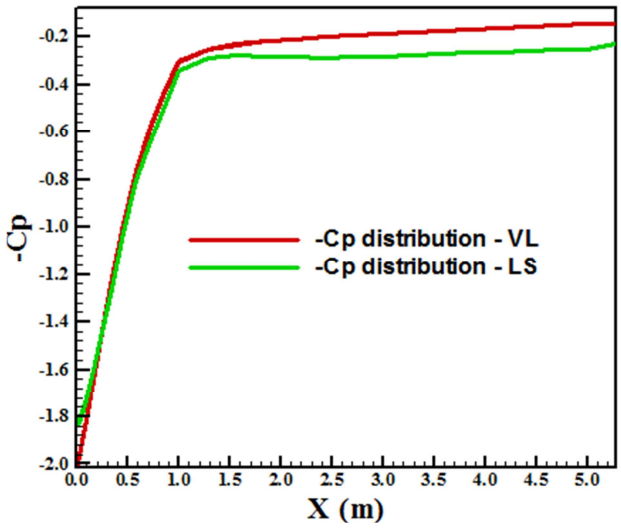

Figure 9. *-Cp distributions.*

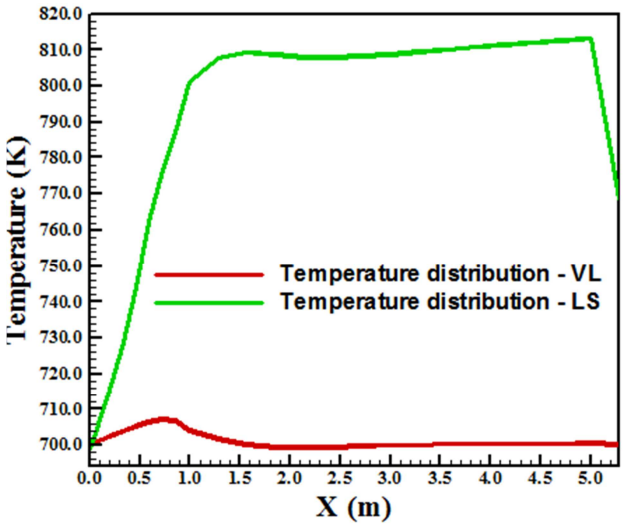

Figure 10. *Wall temperature distributions.*

5.2. Menter and Rumsey Results

The results of this model are divided in its four variants, presented in the following order: Wilcox variant, k-ε variant, BSL variant, and SST variant.

5.2.1. Wilcox Variant

Figure 11 and 12 present the pressure contours obtained by the [2] and [3] schemes, respectively, as using the [11] turbulence model in its Wilcox variant. Again, the pressure contours generated by the [2] scheme is more strength than the one generated by the [3] scheme. Good homogeneity is observed in both solutions, as well good symmetry properties.

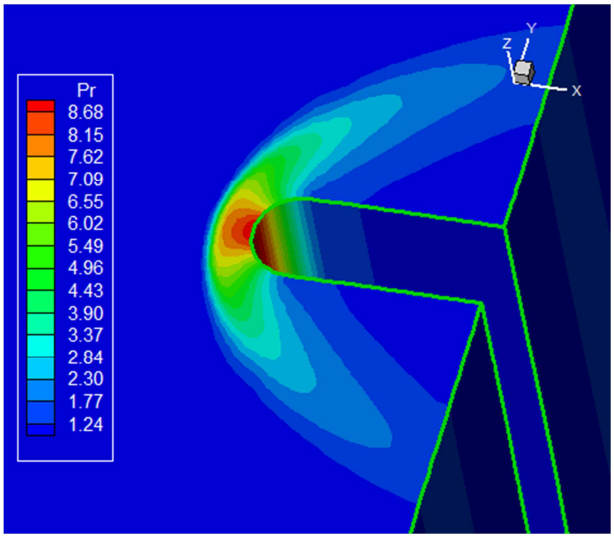

Figure 11. *Pressure contours ([2]).*

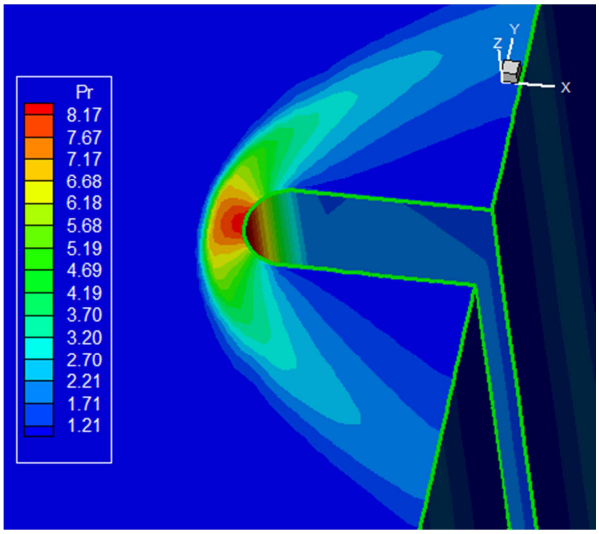

Figure 12. *Pressure contours ([3]).*

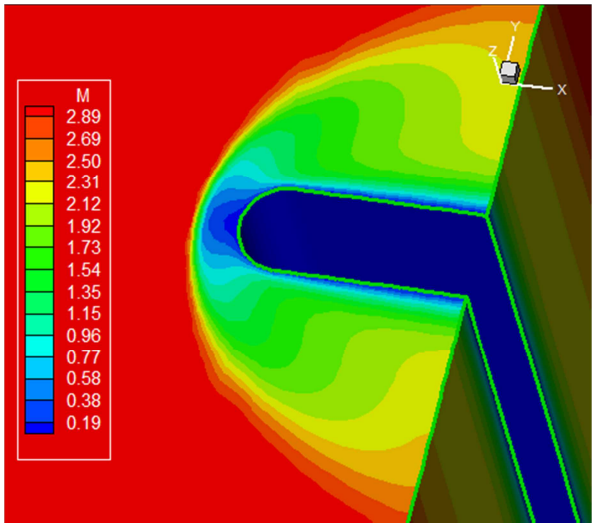

Figure 13. *Mach number contours ([2]).*

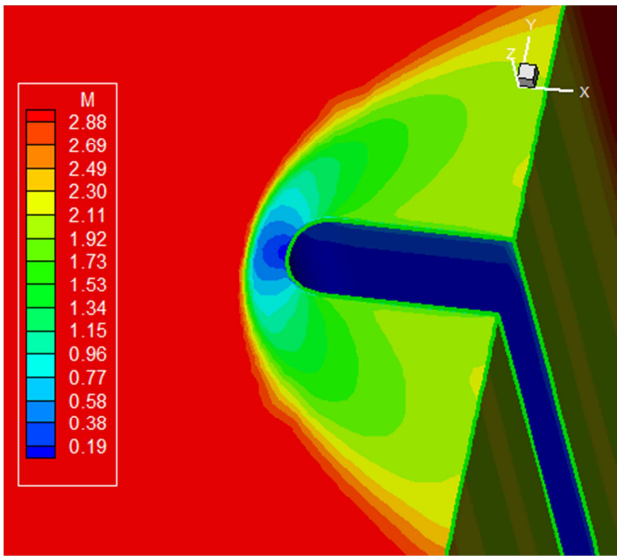

Figure 14. *Mach number contours ([3]).*

Figures 13 and 14 show the Mach number contours generated by the [2] and [3] schemes, respectively, as using the [11] turbulence model in its Wilcox variant. The [2] solution is more intense than the [3] solution. The subsonic region close to the body wall is again observed only in the [2] solution. The subsonic region at the body nose is observed, as resulting from the shock slowdown. No pre-shock oscillations are observed in both solutions.

Figures 15 and 16 exhibit the translational temperature contours obtained by the [2] and [3] schemes, respectively, as using the [11] turbulence model in its Wilcox variant. The [2] solution presents higher temperatures in the field than the [3] solution. Moreover, the [2] solution presents a zone of high dissipation close to body wall, resulting from intense heat energy exchange and boundary layer interaction.

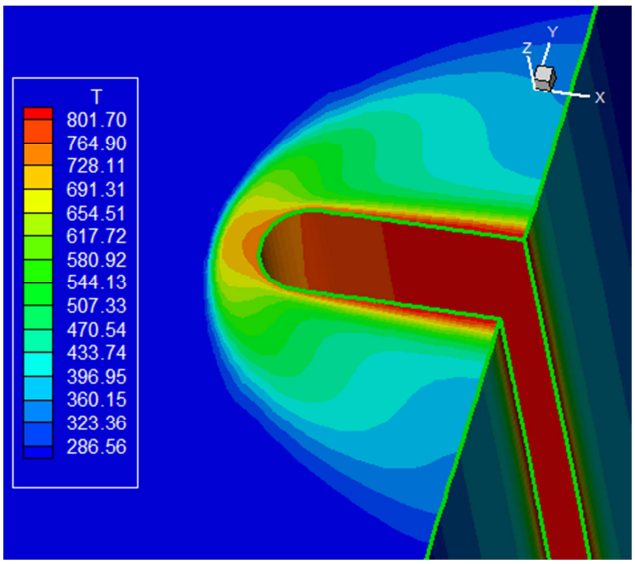

Figure 15. *Temperature contours ([2]).*

Figure 17 presents the –Cp distribution generated by the [2] and [3] schemes as using the [11] turbulence model in its Wilcox variant.

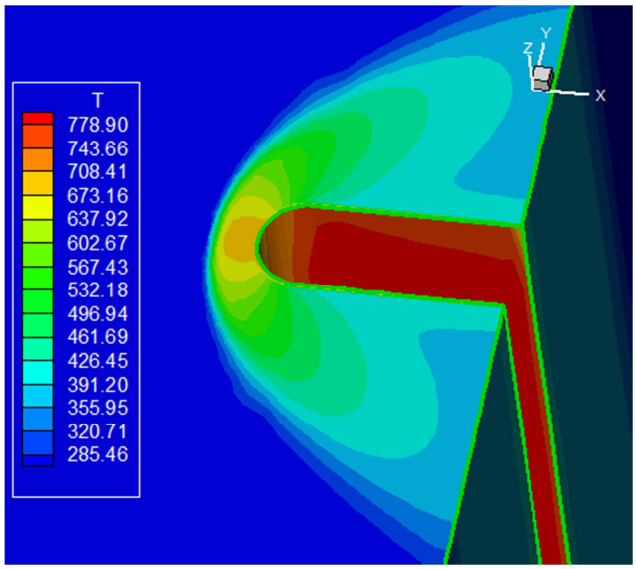

Figure 16. *Temperature contours ([3]).*

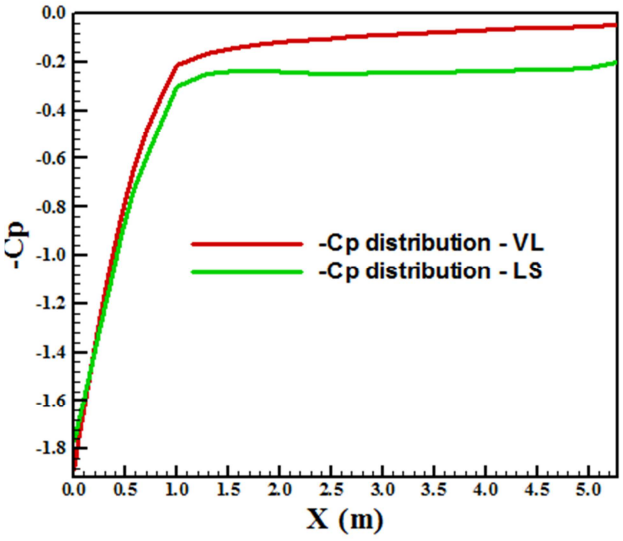

Figure 17. *–Cp distributions.*

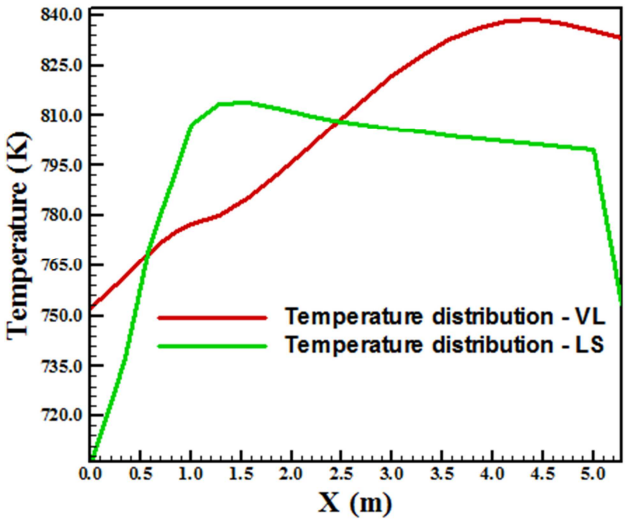

Figure 18. *Wall temperature distributions.*

As can be seen the –Cp plateau obtained by the [2] scheme is higher than the respective one of the [3] scheme. The –Cp peak is approximately the same for both solutions. Figure 18 shows the wall translational temperature distributions originated by the [2] and [3] schemes as using the [11] turbulence model in its Wilcox variant. The [2] temperature distribution is smoother than the [3] one. The temperature at the body nose is higher in the [2] solution. The [2] temperature distribution increases along the body. The [2] temperature at the body nose is 45.0 K higher than the [3] temperature one.

5.2.2. k-ε Variant

Figures 19 and 20 exhibit the pressure contours generated by the [2] and [3] schemes, respectively, as using the [11] turbulence model in its k-ε variant. The pressure field generated by the [2] scheme is higher than the respective one generated by the [3] scheme. Both pressure fields present good homogeneity properties, as well good symmetry properties.

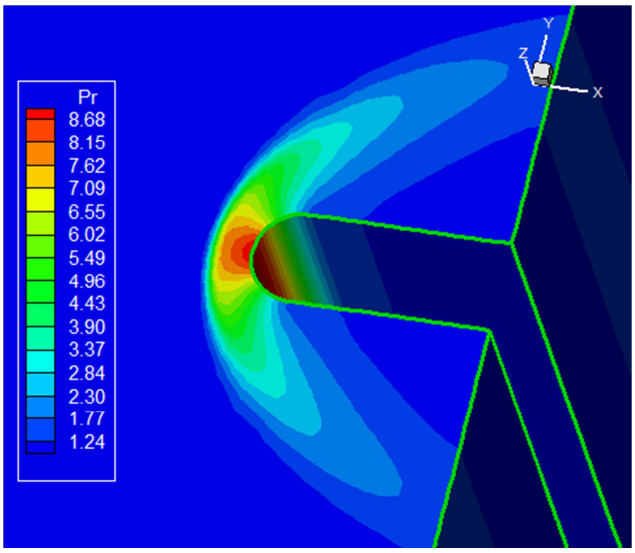

Figure 19. *Pressure contours ([2]).*

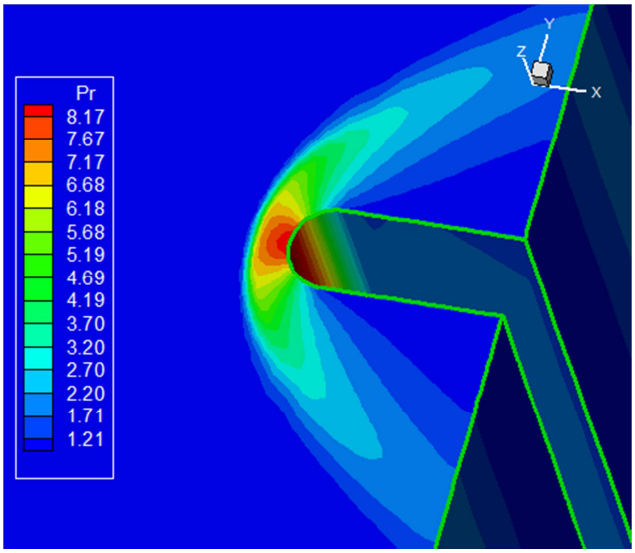

Figure 20. *Pressure contours ([3]).*

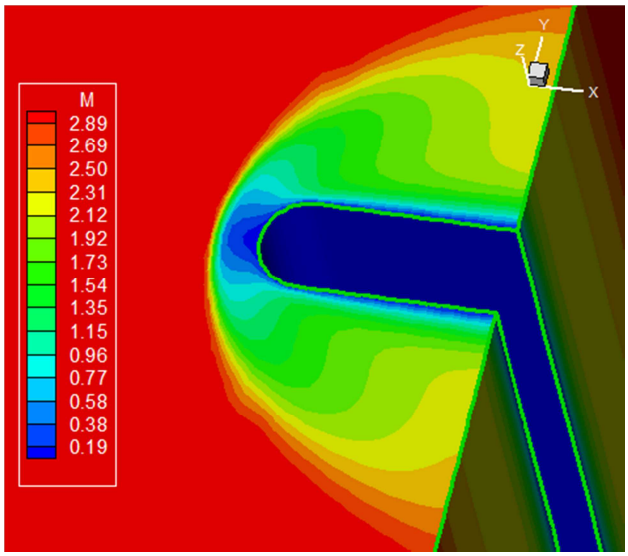

Figure 21. *Mach number contours ([2]).*

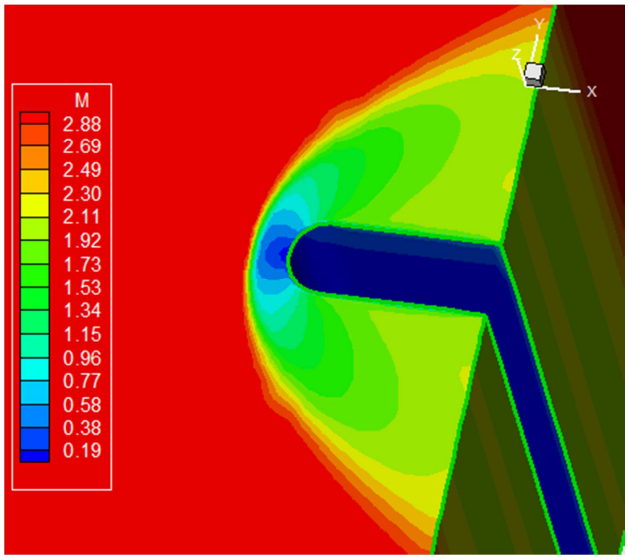

Figure 22. *Mach number contours ([3]).*

Figures 21 and 22 show the Mach number contours obtained by the [2] and [3] schemes, respectively, as using the [11] turbulence model in its k-ε variant. The Mach number field generated by the [2] scheme is more intense than the respective one of the [3] scheme. Particularly, the zone of low Mach number close to the body wall is only perceptible in the [2] solution. The region of subsonic Mach number at the body nose is well captured by both schemes.

Figures 23 and 24 exhibit the translational temperature contours obtained by the [2] and [3] schemes, respectively, as using the [11] turbulence model in its k-ε variant. The temperature field generated by the [2] scheme is again more intense than the respective one of the [3] scheme. Good homogeneous properties are observed in both figures. The zone of intense energy exchange, close to the body wall, is observed in the [2] solution. Moreover, the zone of intense temperature is slightly observed at the body nose in both solutions. Good symmetry properties are noted in both figures.

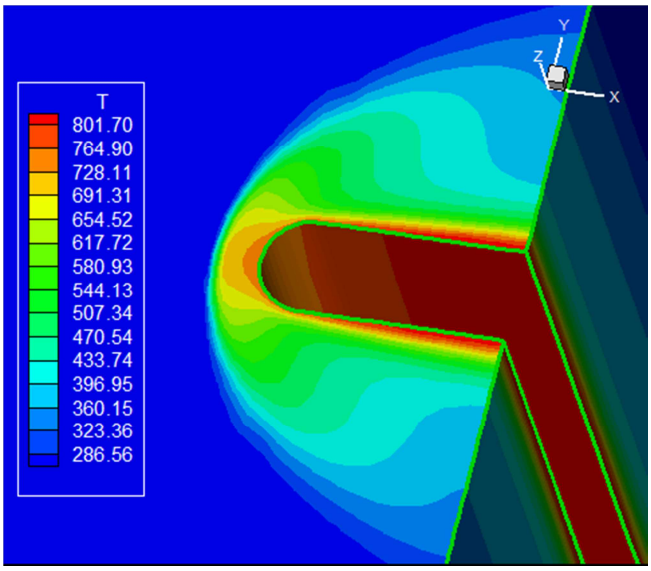

Figure 23. *Temperature contours ([2]).*

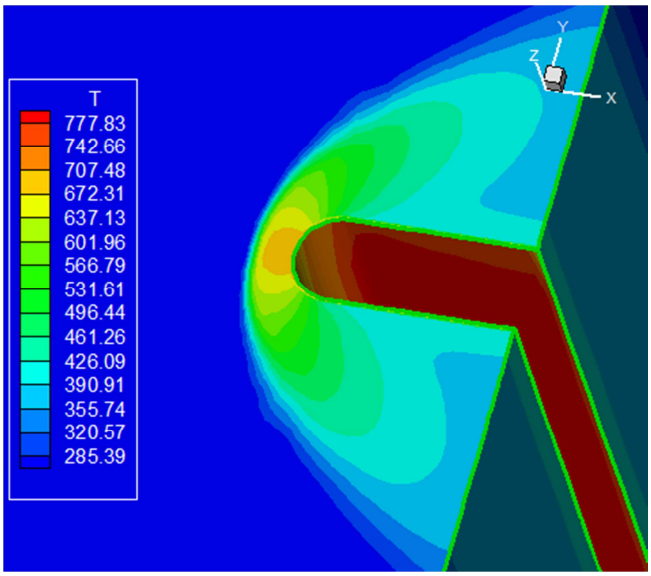

Figure 24. *Temperature contours ([3]).*

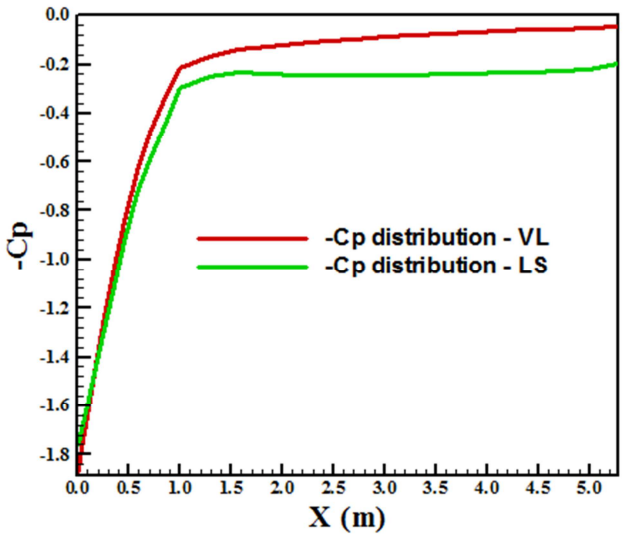

Figure 25. *–Cp distributions.*

Figure 25 presents the –Cp distribution obtained by the [2] and [3] schemes as using the [11] turbulence model in its k-ε variant. In accordance to the observed in the ultimate solutions, the [2] scheme presents higher –Cp plateau than the [3] scheme; Moreover, both solutions present the same –Cp peak, at the body nose. Figure 26 shows the wall temperature distributions obtained by the [2] and [3] schemes as using the [11] turbulence model in its k-ε variant. Both solutions present different temperature peaks at the leading edge, the difference around 45.0 K. Again the [2] solution presents an increase of the temperature along the body, whereas the [3] solution suffers an increase and posteriorly a reduction of temperature. The maximum temperature reached by the [2] scheme is about 840.0 K, whereas by the [3] scheme is 816.0 K.

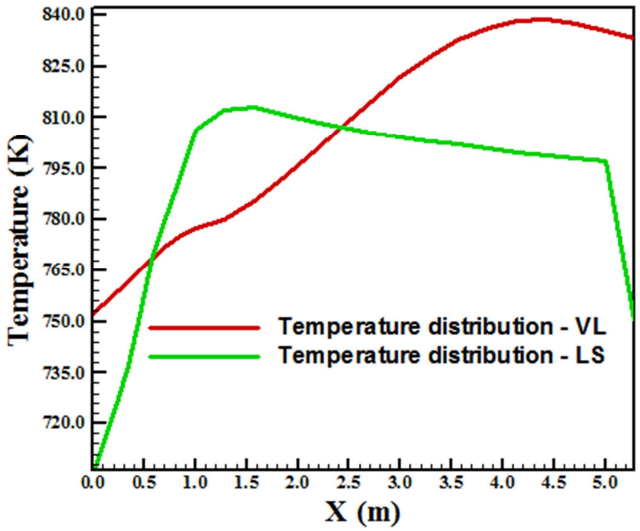

Figure 26. *Wall temperature distributions.*

5.2.3. BSL Variant

Figures 27 and 28 exhibit the pressure contours generated by the [2] and [3] schemes, respectively, as using the [11] turbulence model in its BSL variant. The pressure field generated by the [2] scheme is higher than the respective one generated by the [3] scheme. Both pressure fields present good homogeneity properties, as well good symmetry properties. Some problems in the [3] solution are related with the no repetition of the solution in all k planes. It was noted before and it repeats now. It is important to note that the [2] solution does not present such problem.

Figures 29 and 30 show the Mach number contours obtained by the [2] and [3] schemes, respectively, as using the [11] turbulence model in its BSL variant. The Mach number field generated by the [2] scheme is more intense than the respective one of the [3] scheme. Particularly, the zone of low Mach number close to the body wall is only perceptible in the [2] solution. The region of subsonic Mach number at the body nose is well captured by both schemes. Not pre-shock oscillations are observed in the solutions. Good symmetry and homogenous properties are noted in both figures.

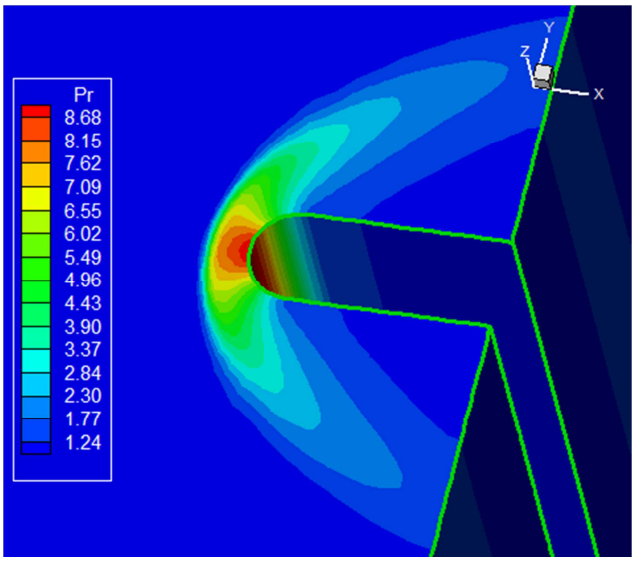

Figure 27. *Pressure contours ([2]).*

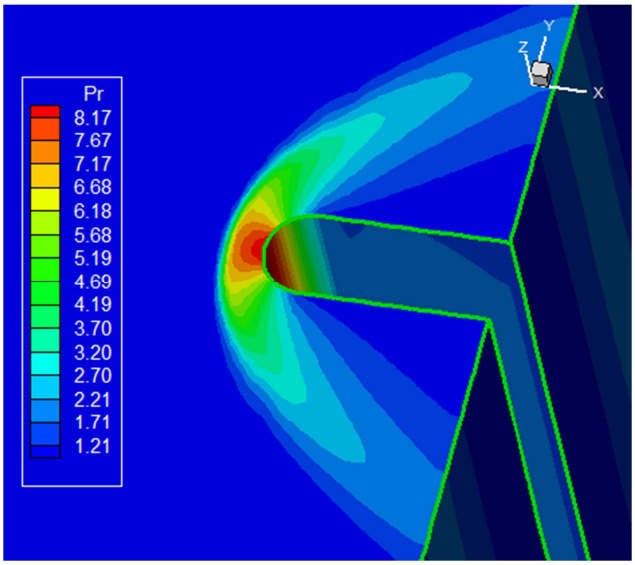

Figure 28. *Pressure contours ([3]).*

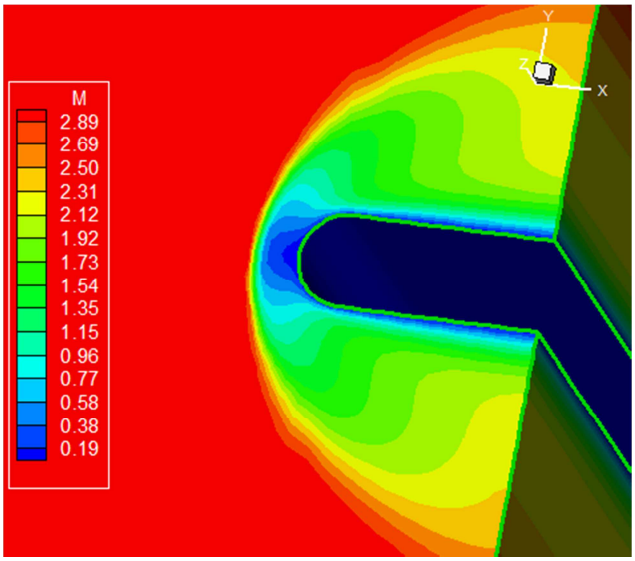

Figure 29. *Mach number contours ([2]).*

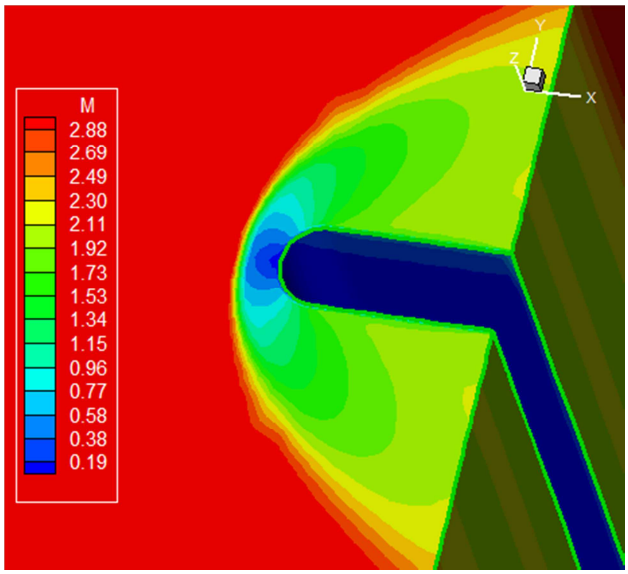

Figure 30. *Mach number contours ([3]).*

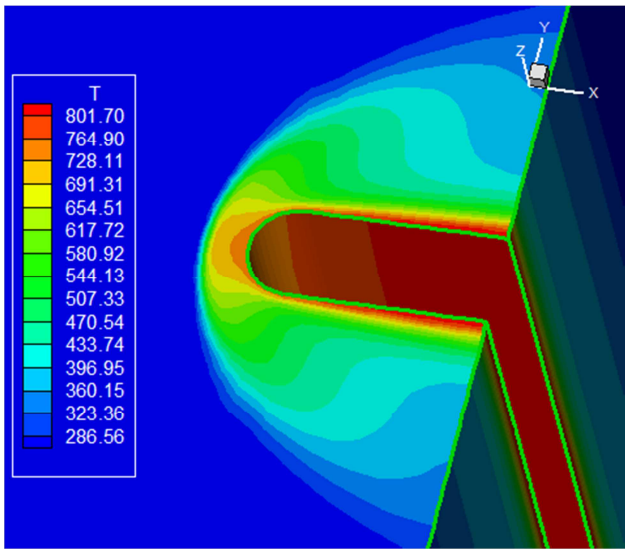

Figure 31. *Temperature contours ([2]).*

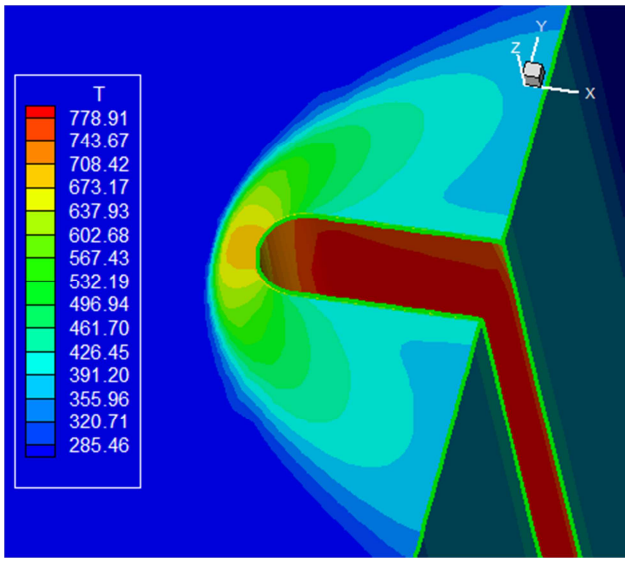

Figure 32. *Temperature contours ([3]).*

Figures 31 and 32 exhibit the translational temperature contours obtained by the [2] and [3] schemes, respectively, as using the [11] turbulence model in its BSL variant. The temperature field generated by the [2] scheme is again more intense than the respective one of the [3] scheme. Good homogeneous properties are observed in both figures. The zone of intense energy exchange, close to the body wall, is observed in the [2] solution. Moreover, the zone of intense temperature is slightly observed at the body nose in both solutions. Good symmetry properties are noted in both figures.

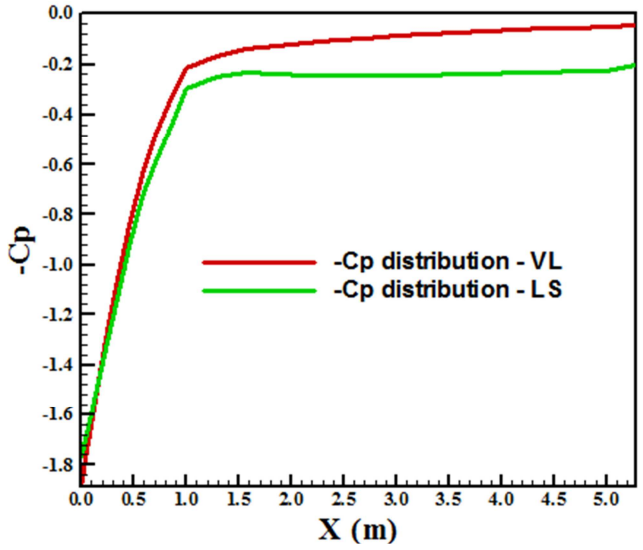

Figure 33. *–Cp distributions.*

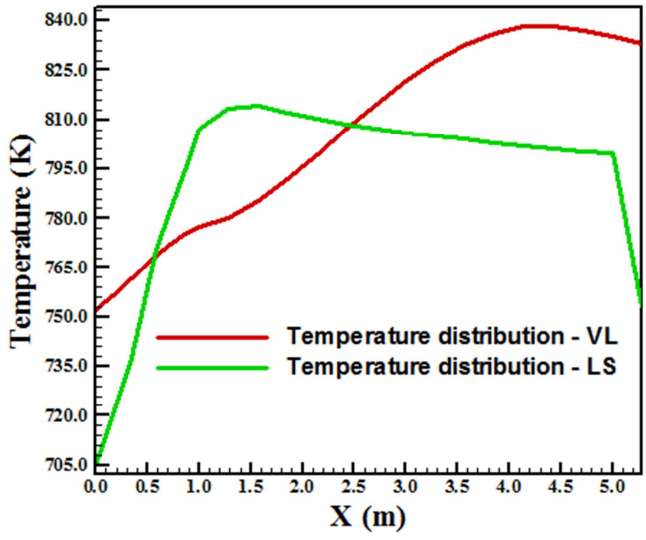

Figure 34. *Wall temperature distributions.*

Figure 33 presents the –Cp distribution obtained by the [2] and [3] schemes as using the [11] turbulence model in its BSL variant. In accordance to the observed in the ultimate solutions, the [2] scheme presents higher –Cp plateau than the [3] scheme; Moreover, both solutions present the same –Cp peak, at the body nose. Figure 34 shows the wall temperature distributions obtained by the [2] and [3] schemes as using the [11] turbulence model in its BSL variant. Both solutions present different temperature peaks at the leading edge, the difference around 45.0 K. Again the [2] solution presents an increase of the temperature along the body, whereas the [3] solution suffers an increase and posteriorly a reduction of temperature. The maximum temperature reached by the [2] scheme is near 840.0 K, whereas by the [3] scheme is 816.0 K.

5.2.4. SST Variant

Figures 35 and 36 present the pressure contours obtained by the [2] and [3] schemes, respectively, as using the [11] turbulence model in its SST variant in three-dimensions. Both fields are homogeneous and the pressure contours generated by the [2] scheme is more strength than the respective one generated by the [3] scheme. Good symmetry properties are observed in both figures. The shock wave is well captured by both schemes as using the [11] turbulence model in its SST variant.

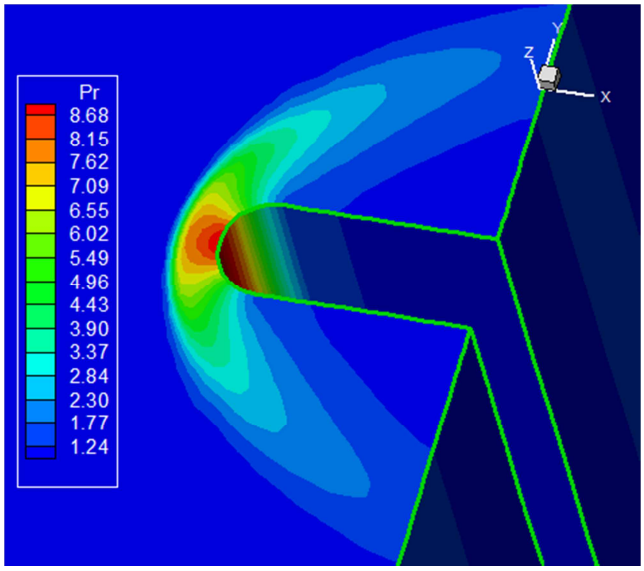

Figure 35. *Pressure contours ([2]).*

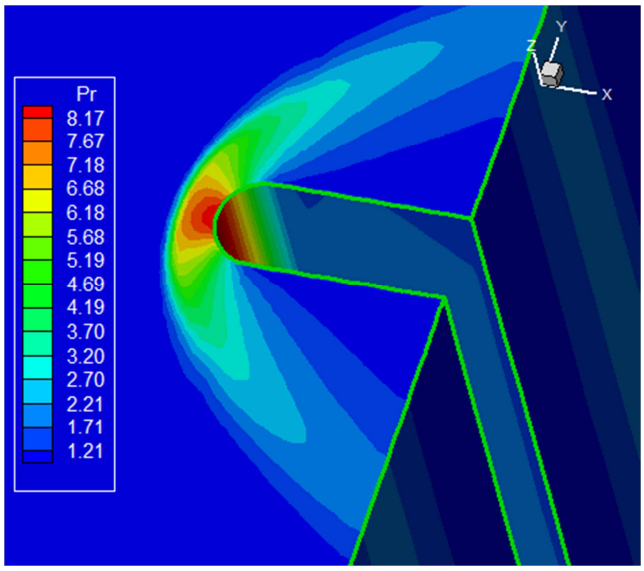

Figure 36. *Pressure contours ([3]).*

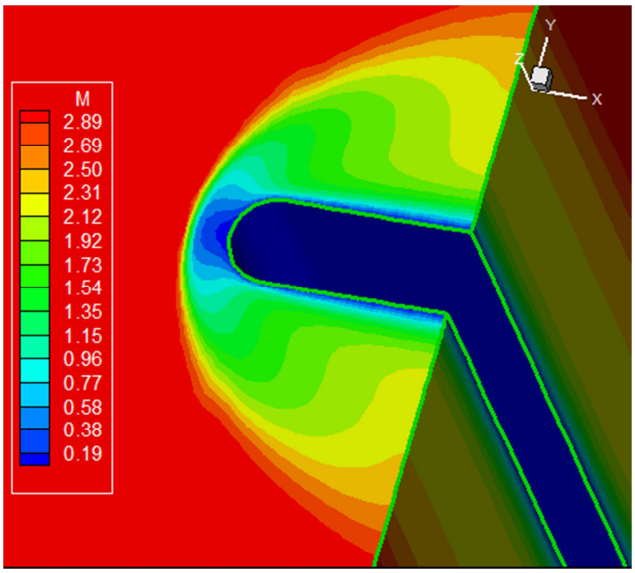

Figure 37. *Mach number contours ([2]).*

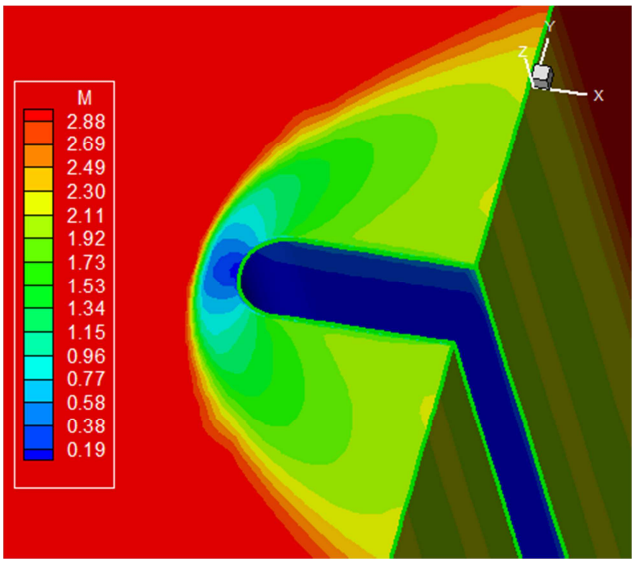

Figure 38. *Mach number contours ([3]).*

Figures 37 and 38 show the Mach number contours obtained by the [2] and [3] numerical schemes, respectively, as using the [11] turbulence model in its SST variant. Both Mach number fields are free of pre-shock oscillations and are homogeneous. The Mach number field generated by the [2] scheme is slightly more intense than that of the [3] scheme. It is possible to see that the [2] solution develops a region of low Mach number contours close to the wall, resulting from the boundary layer formation. On the contrary, the [3] solution does not yields this region.

Figures 39 and 40 exhibit the translational temperature contours obtained by the [2] and [3] schemes, respectively, as using the [11] turbulence model in its SST variant. The temperature contours generated by the [2] scheme is again more intense than the respective one of the [3] scheme. The [2] solution presents a zone of high dissipation close to the wall, whereas the [3] scheme does not. There are qualitative differences between the two solutions, but both present homogeneous contours, without oscillations. Some problems with the [3] solution in the k = constant planes are observed, which prejudices the solution repetition in these planes. The [2] solution does not present such problems.

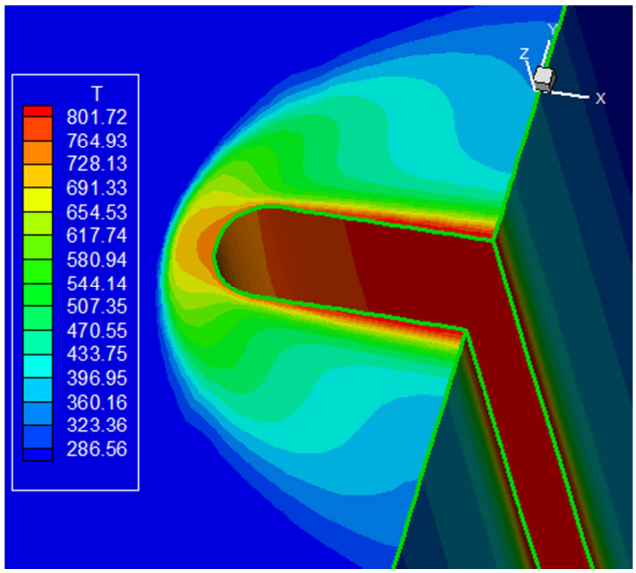

Figure 39. *Temperature contours ([2]).*

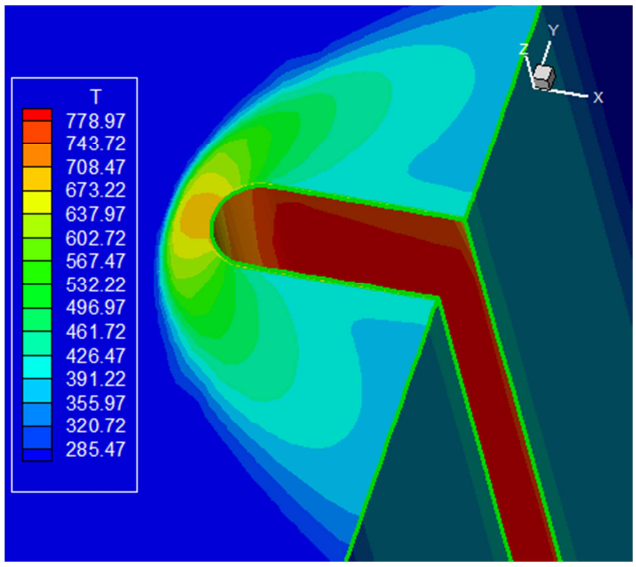

Figure 40. *Temperature contours ([3]).*

Figure 41 exhibits the -Cp distributions generated by the [2] and [3] schemes as using the [11] turbulence model in its SST variant. The -Cp plateau of the [2] scheme is again higher than the -Cp plateau of the [3] scheme. The -Cp peak at the body nose is approximately the same for both schemes. Figure 42 presents the wall temperature distributions generated by the [2] and [3] numerical schemes as using the [11] turbulence model in its SST variant. The temperature distribution is smoother for the [2] scheme. The temperature distribution of the [2] scheme is more intense than the respective one of the [3] scheme. The maximum temperature obtained by the [2] scheme is about 840.0 K, whereas that obtained by the [3] scheme is about 819.0 K.

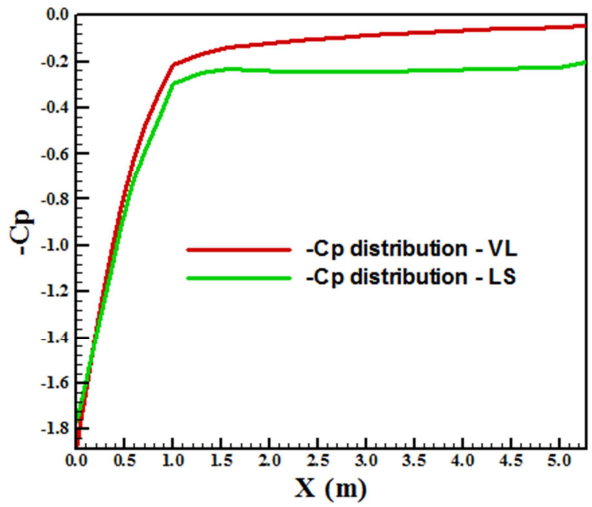

Figure 41. *–Cp distributions.*

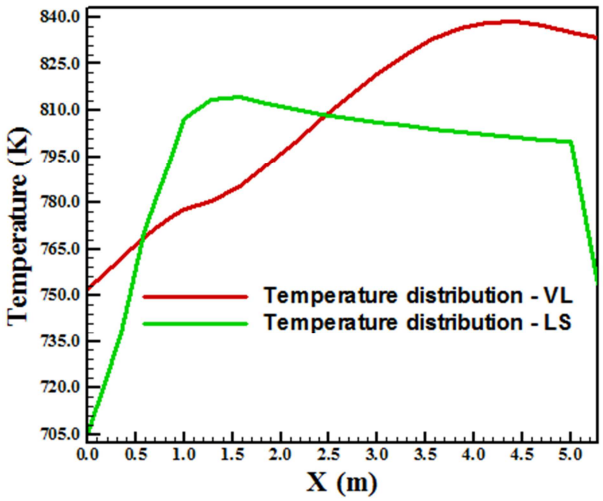

Figure 42. *Wall temperature distributions.*

5.3. Gibson and Dafa'Alla Results

These results are presented in the four variants of the [12] turbulence models.

5.3.1. Launder and Sharma Option to Constants and f_μ

Figures 43 and 44 exhibit the pressure contours generated by the [2] and [3] schemes, respectively, as using the [12] turbulence model in its LS-LS variant. The pressure field generated by the [2] scheme is higher than the respective one generated by the [3] scheme. Both pressure fields present good homogeneity properties, as well good symmetry properties.

Figures 45 and 46 show the Mach number contours obtained by the [2] and [3] schemes, respectively, as using the [12] turbulence model in its LS-LS variant. The Mach number field generated by the [2] scheme is the same in relation to the respective one of the [3] scheme, in quantitative terms. The differences are in qualitative terms. Particularly, the zone of low Mach number close to the body wall is only perceptible in the [2] solution. The region of subsonic Mach number at the body nose is well captured by both schemes. No pre-shock oscillations are observed in both figures. The shock wave is well captured in both solutions. Good homogeneous and symmetry properties are observed in both solutions.

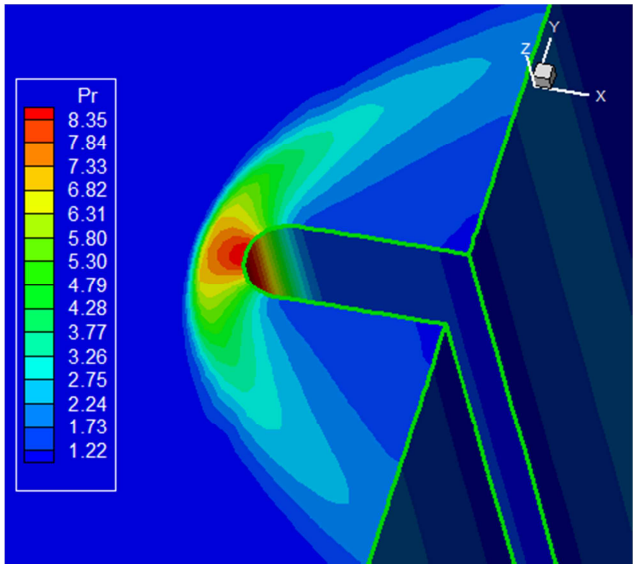

Figure 43. *Pressure contours ([2]).*

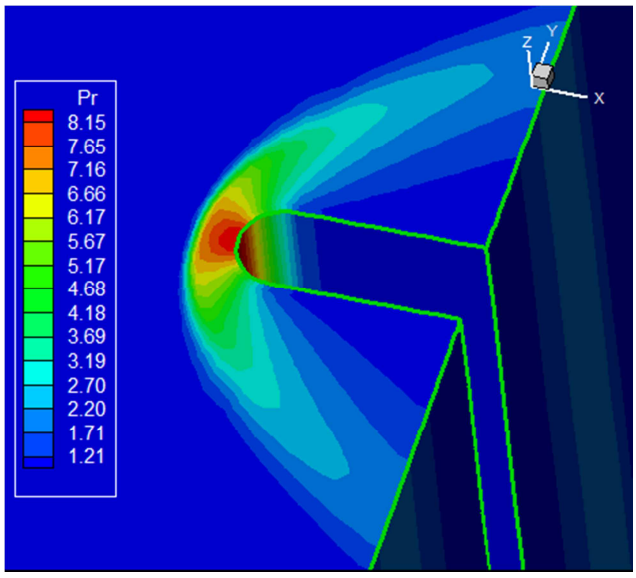

Figure 44. *Pressure contours ([3]).*

Figures 47 and 48 exhibit the translational temperature contours obtained by the [2] and [3] schemes, respectively, as using the [12] turbulence model in its LS-LS variant. The temperature field generated by the [3] scheme is more intense than the respective one of the [2] scheme. Good homogeneous properties are observed in both figures. The zone of intense energy exchange, close to the body wall, is observed only in the [2] solution. Moreover, the zone of intense temperature is slightly observed at the body nose in both solutions. Good symmetry properties are noted in both solutions.

Figure 49 presents the –Cp distribution obtained by the [2] and [3] schemes as using the [12] turbulence model in its LS-LS variant.

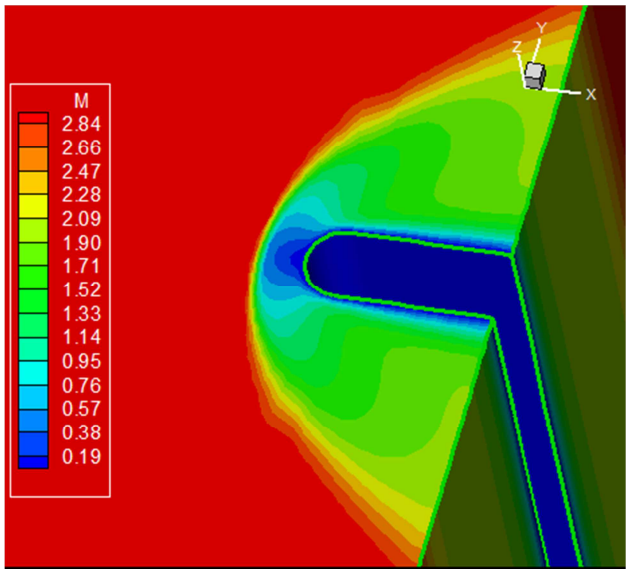

Figure 45. *Mach number contours ([2]).*

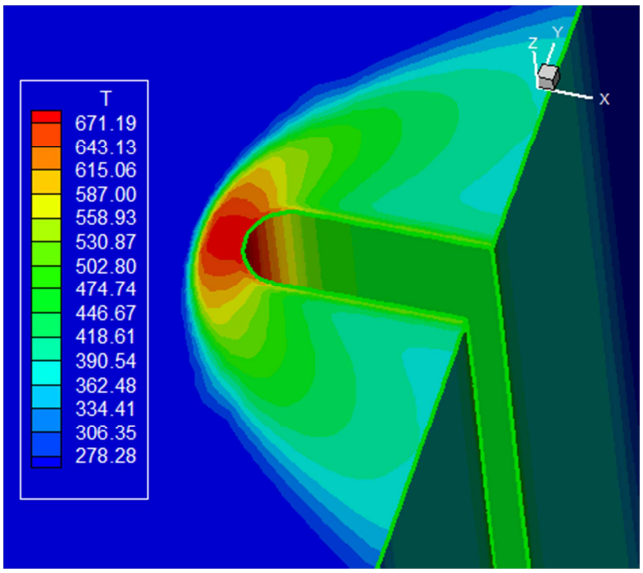

Figure 48. *Temperature contours ([3]).*

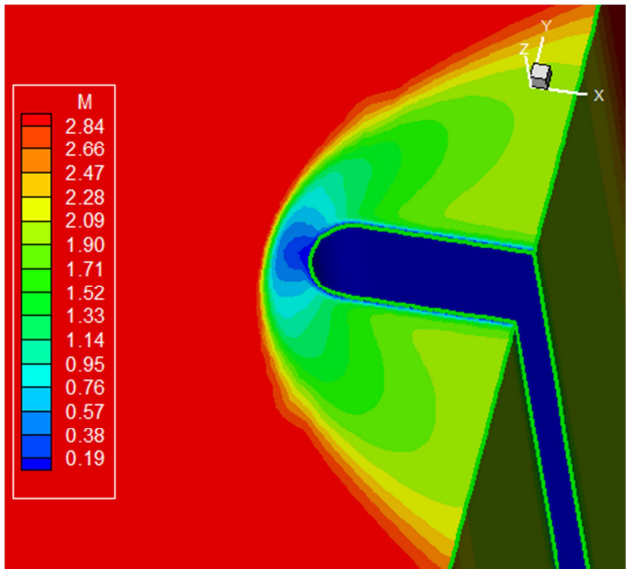

Figure 46. *Mach number contours ([3]).*

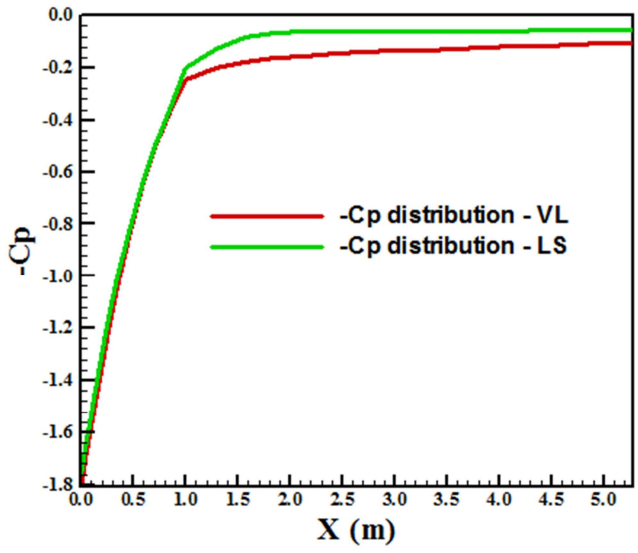

Figure 49. *–Cp distributions.*

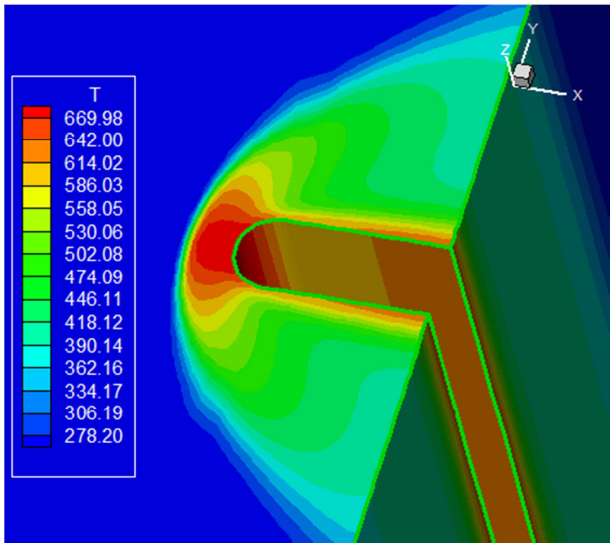

Figure 47. *Temperature contours ([2]).*

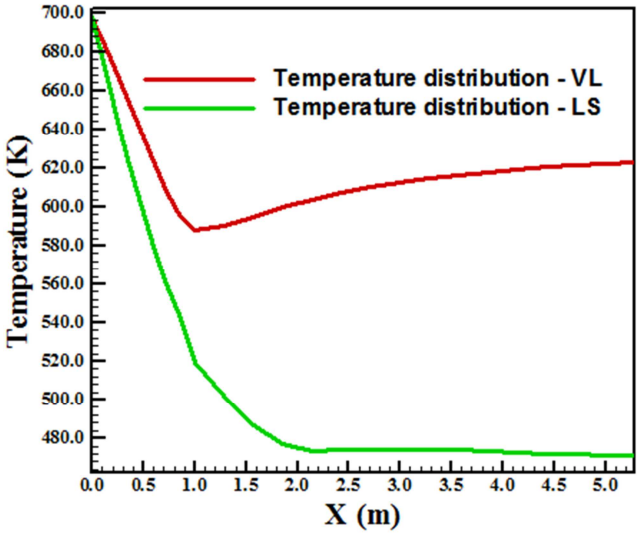

Figure 50. *Wall temperature distributions.*

Opposed to the observed in the ultimate solutions, the [3] scheme presents higher –Cp plateau than the [2] scheme; Moreover, both solutions present the same –Cp peak, at the body's nose.

Figure 50 shows the wall temperature distributions obtained by the [2] and [3] schemes as using the [12] turbulence model in its LS-LS variant. Both solutions present the same temperature peaks at the leading edge. The [3] solution presents a decrease of temperature along the body, whereas the [2] solution suffers a reduction and an increase of temperature along the body.

5.3.2. Launder and Sharma Option to Constants and Chien to f_μ

Figures 51 and 52 show the pressure contours obtained by the [2] and [3] schemes, respectively, as using the [12] turbulence model in its LS-C variant. As can be observed, the [2] scheme predicts again more severe pressure field than the [3] scheme. The shock is well capture and good symmetry characteristics are noted. Good homogeneity in both solutions is also observed.

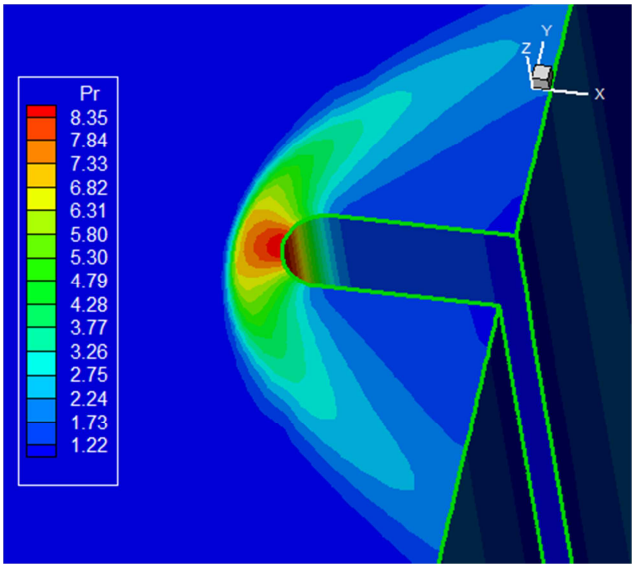

Figure 51. *Pressure contours ([2]).*

Figures 53 and 54 present the Mach number contours generated by the [2] and [3] schemes, respectively, as using the [12] turbulence model in its LS-C variant. Good symmetry properties are observed, without pre-shock oscillations. Good homogeneity properties are noted. The Mach number fields are identical in quantitative terms, although in qualitative terms some discrepancies are observed. The zone of low Mach number close to the body wall is only noted in the [2] solution.

Figures 55 and 56 show the translational temperature contours obtained by the [2] and [3] schemes, respectively, as using the [12] turbulence model in its LS-C variant. As can be observed, the [3] temperature field is more intense than the [2] temperature field. The zone of intense energy exchange observed close to the body wall is only captured by the [2] scheme. Moreover, the intense temperature region at the body nose is observed in both solutions.

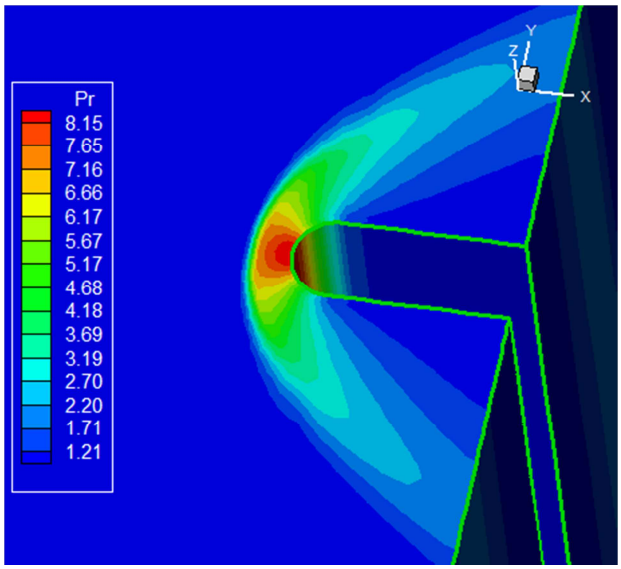

Figure 52. *Pressure contours ([3]).*

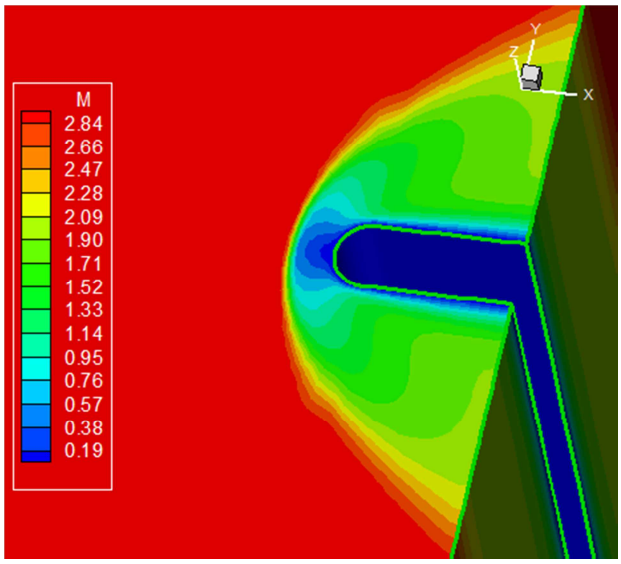

Figure 53. *Mach number contours ([2]).*

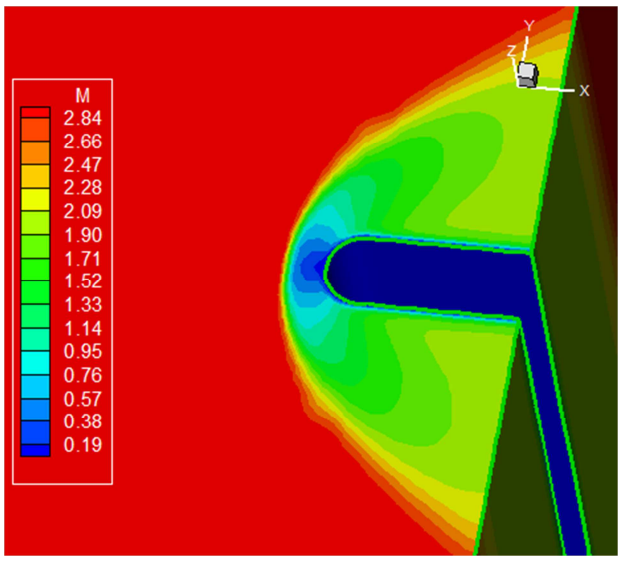

Figure 54. *Mach number contours ([3]).*

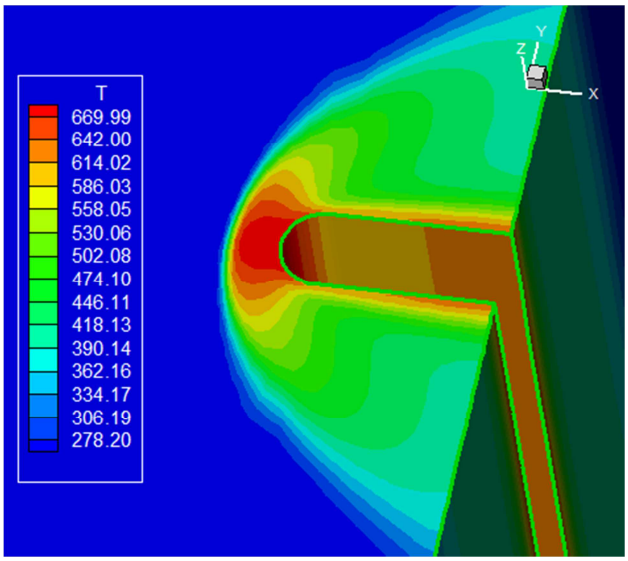

Figure 55. *Temperature contours ([2]).*

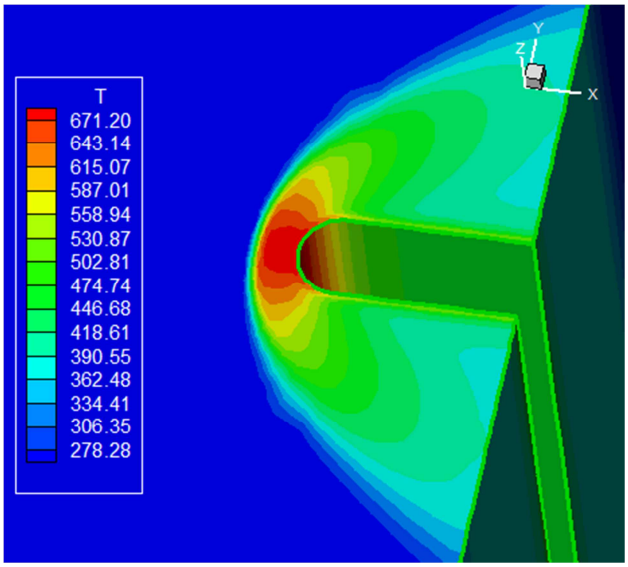

Figure 56. *Temperature contours ([3]).*

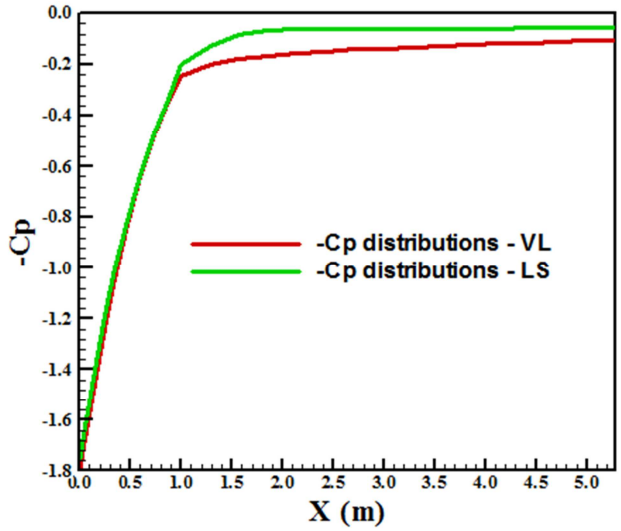

Figure 57. *–Cp distributions.*

Figure 57 exhibits the –Cp distributions at the wall obtained by the [2] and [3] schemes as using the [12] turbulence model in its LS-C variant. As observed in the [12] solutions, the [3] scheme presents again a pressure plateau higher than the [2] scheme does, although both –Cp peaks at the body nose are approximately the same. Figure 58 shows the temperature distributions at wall generated by the [2] and [3] schemes as using the [12] turbulence model in its LS-C variant. The [3] temperature distributions is smoother than the [2] one. The [2] temperature distribution decreases and increases along the body, whereas the [3] temperature distribution decreases until reach a constant value. The temperature values at the body end are approximately 620.0 K to the [2] scheme and 470.0 K to the [3] scheme. The maximum temperature value, at the body leading edge, for both solutions is 700.0 K.

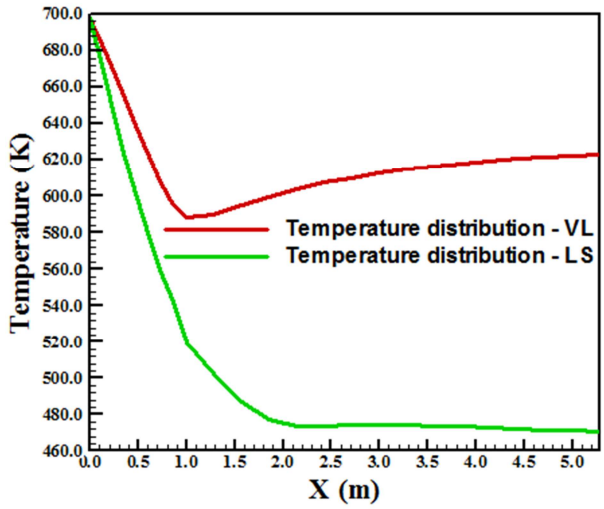

Figure 58. *Wall temperature distributions.*

5.3.3. Chien Option to Constants and Launder and Sharma to f_μ

Figures 59 and 60 show the pressure contours obtained by the [2] and [3] schemes, respectively, as using the [12] turbulence model in its C-LS variant. As can be observed, the [2] scheme predicts again more severe pressure field than the [3] scheme. The shock is well capture and good symmetry characteristics are noted. Good homogeneity in both solutions is also observed.

Figures 61 and 62 present the Mach number contours generated by the [2] and [3] schemes, respectively, as using the [12] turbulence model in its C-LS variant. Good symmetry properties are observed, without pre-shock oscillations. Good homogeneity properties are noted. The Mach number fields are identical in quantitative terms, although in qualitative terms some discrepancies are observed. The zone of low Mach number close to the body wall is only noted in the [2] solution. The subsonic region located at the body nose is captured by both schemes.

Figures 63 and 64 show the translational temperature contours obtained by the [2] and [3] schemes, respectively, as using the [12] turbulence model in its C-LS variant.

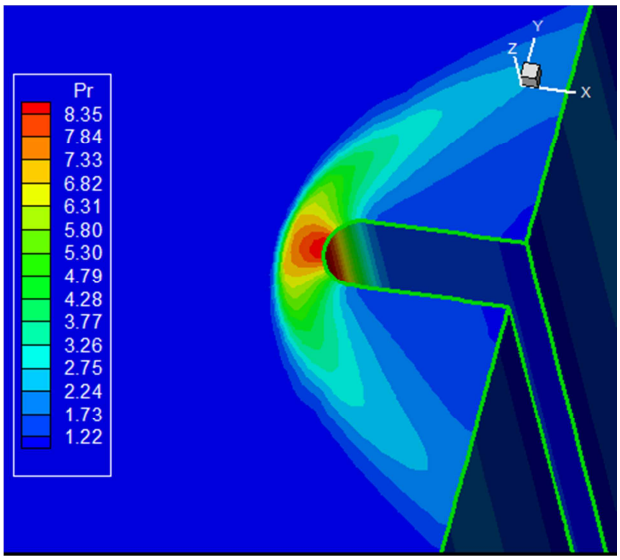

Figure 59. *Pressure contours ([2]).*

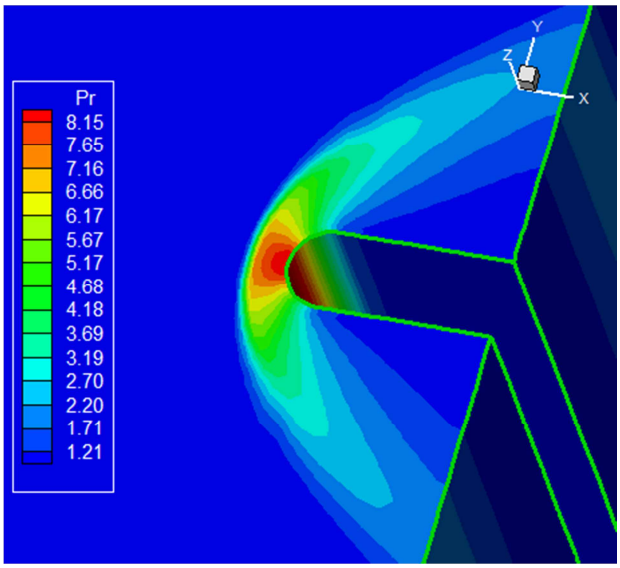

Figure 60. *Pressure contours ([3]).*

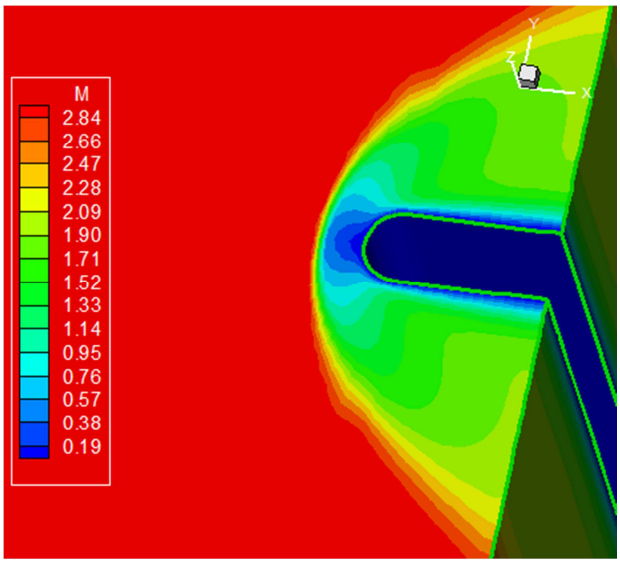

Figure 61. *Mach number contours ([2]).*

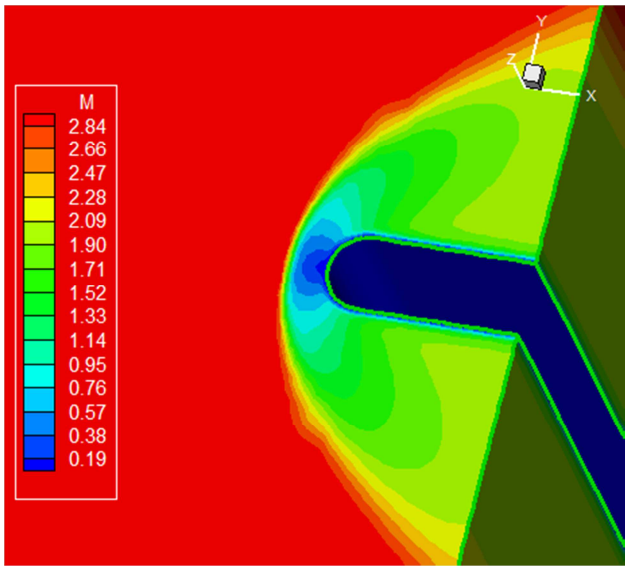

Figure 62. *Mach number contours ([3]).*

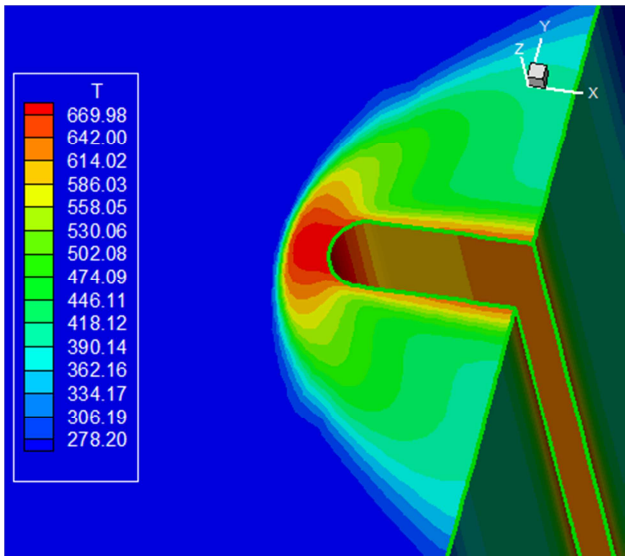

Figure 63. *Temperature contours ([2]).*

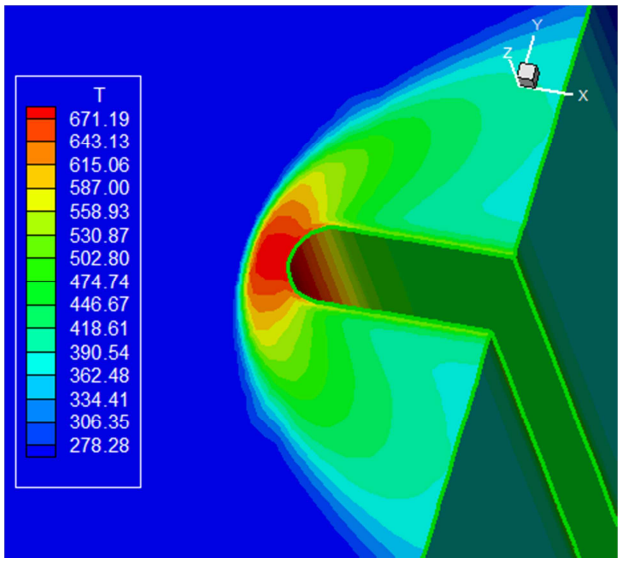

Figure 64. *Temperature contours ([3]).*

As can be observed, the [3] temperature field is more intense than the [2] temperature field. The zone of intense energy exchange observed close to the body wall is again only captured by the [2] scheme. Moreover, the intense temperature region at the body nose is observed in both solutions. Good symmetry properties are noted in both figures.

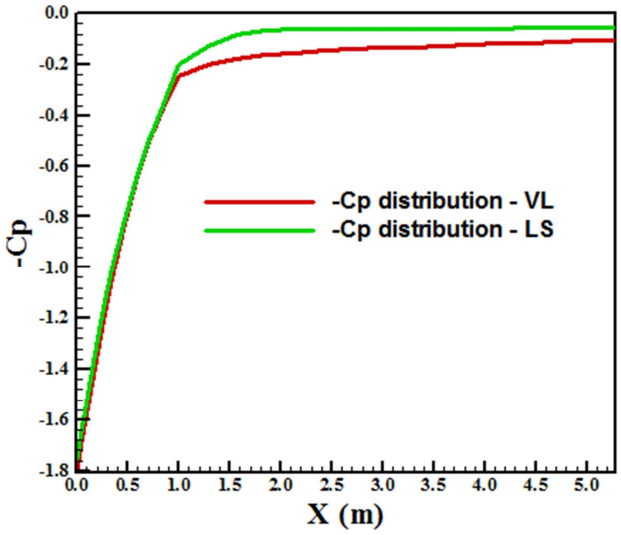

Figure 65. *–Cp distributions.*

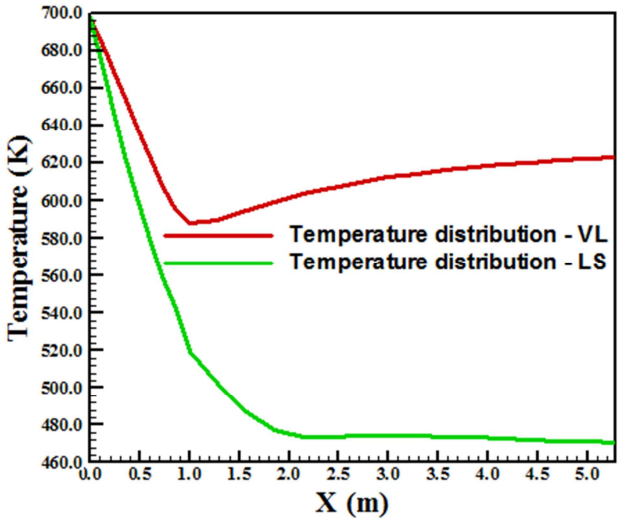

Figure 66. *Wall temperature distributions.*

Figure 65 exhibits the –Cp distributions at the wall obtained by the [2] and [3] schemes as using the [12] turbulence model in its C-LS variant. As observed in the [12] solutions, the [3] scheme presents again a pressure plateau higher than the [2] scheme does, although both –Cp peaks at the body nose are approximately the same. Figure 66 shows the temperature distributions at wall generated by the [2] and [3] schemes as using the [12] turbulence model in its C-LS variant. The [3] temperature distributions is smoother than the [2] one. The [2] temperature distribution decreases and increases along the body, whereas the [3] temperature distribution decreases until reach a constant value. The temperature values at the body end are approximately 620.0 K to the [2] scheme and 470.0 K to the [3] scheme. The maximum temperature value, at the body leading edge, for both solutions is 700.0 K.

5.3.4. Chien Options to Constants and f_μ

Figures 67 and 68 show the pressure contours obtained by the [2] and [3] schemes, respectively, as using the [12] turbulence model in its C-C variant. As can be observed, the [2] scheme predicts again more severe pressure field than the [3] scheme. This behavior has occurred in all solutions in this work. The shock is well capture and good symmetry characteristics are noted. Good homogeneity in both solutions is also observed.

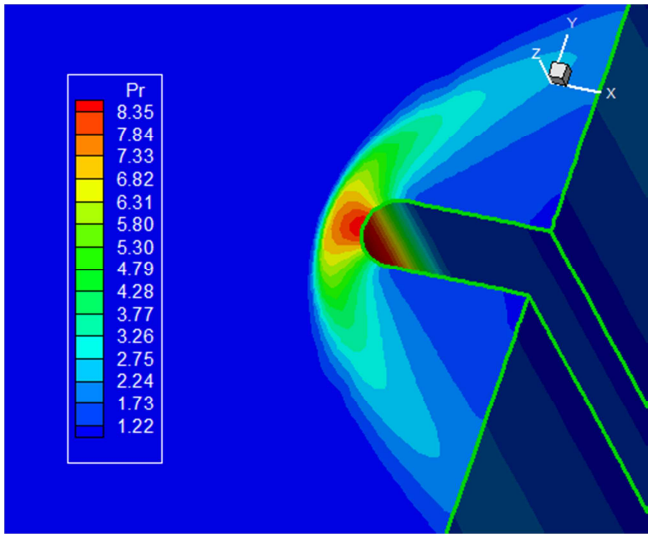

Figure 67. *Pressure contours ([2]).*

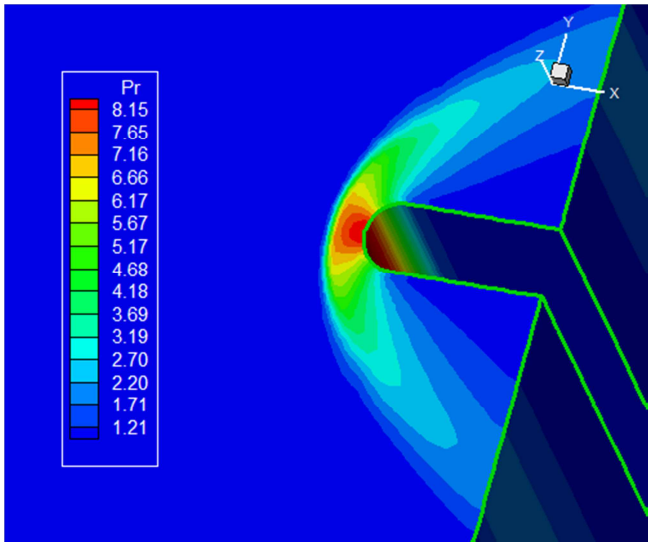

Figure 68. *Pressure contours ([3]).*

Figures 69 and 70 present the Mach number contours generated by the [2] and [3] schemes, respectively, as using the [12] turbulence model in its C-C variant. Good symmetry properties are observed, without pre-shock oscillations. Good homogeneity properties are noted. The Mach number fields are identical in quantitative terms, although in qualitative terms some discrepancies are observed.

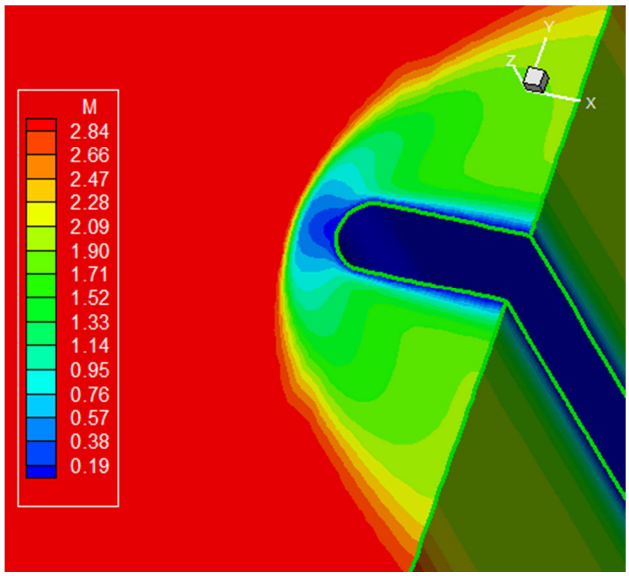

Figure 69. *Mach number contours ([2]).*

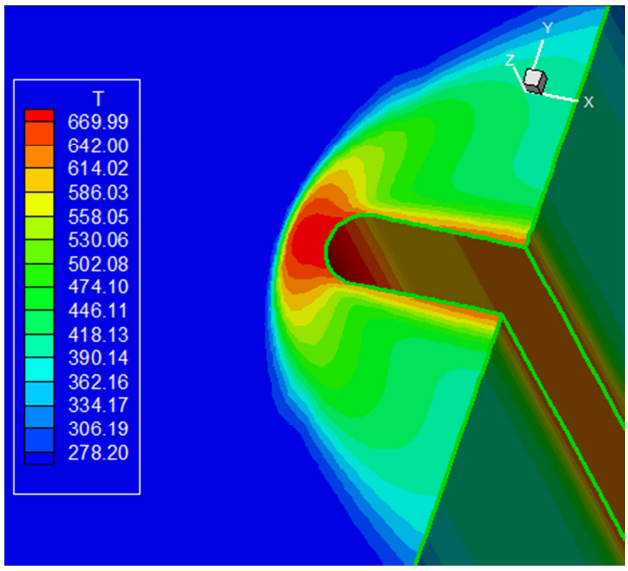

Figure 71. *Temperature contours ([2]).*

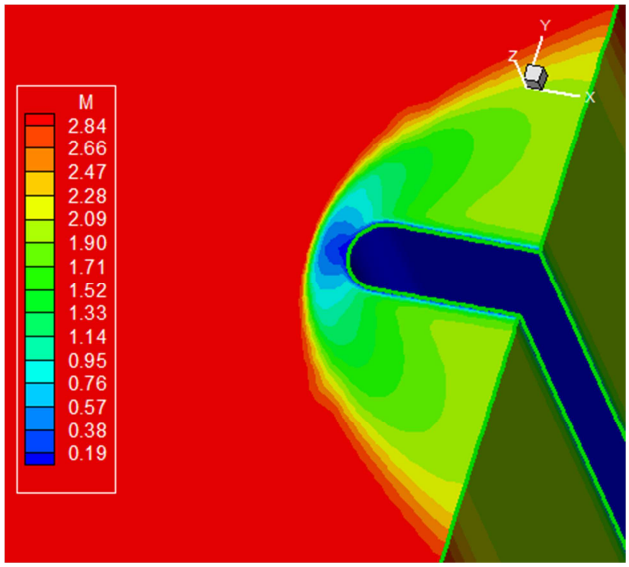

Figure 70. *Mach number contours ([3]).*

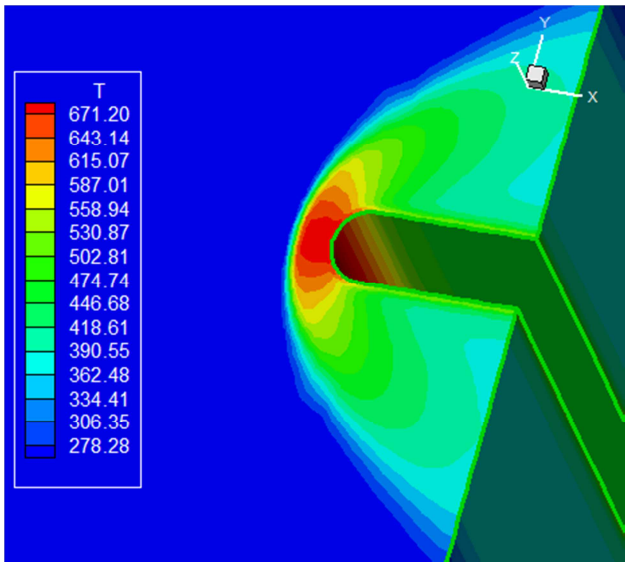

Figure 72. *Temperature contours ([3]).*

The zone of low Mach number close to the body wall is only noted in the [2] solution. The subsonic region located at the body nose is captured by both schemes.

Figures 71 and 72 show the translational temperature contours obtained by the [2] and [3] schemes, respectively, as using the [12] turbulence model in its C-C variant. As can be observed, the [3] temperature field is again more intense than the [2] temperature field. The zone of intense energy exchange observed close to the body wall is again only captured by the [2] scheme. Moreover, the intense temperature region at the body nose is observed in both solutions. Good symmetry properties are noted in both figures.

Figure 73 exhibits the –Cp distributions at the wall obtained by the [2] and [3] schemes as using the [12] turbulence model in its C-C variant. As observed in the [12] solutions, the [3] scheme presents again a pressure plateau higher than the [2] scheme does, although both –Cp peaks at the body nose are approximately the same.

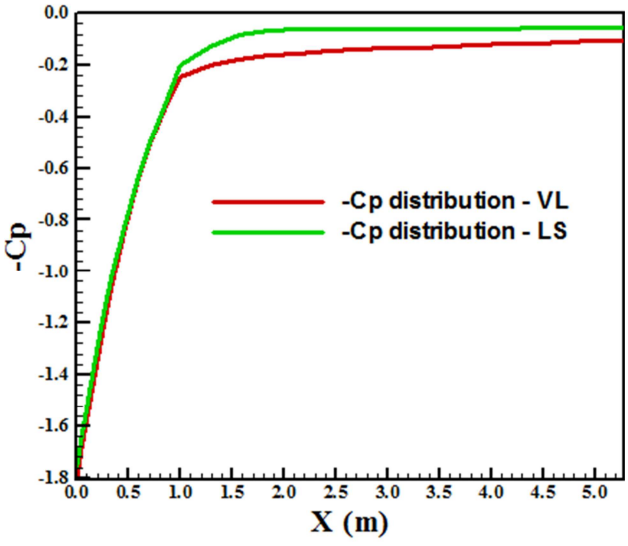

Figure 73. *–Cp distributions.*

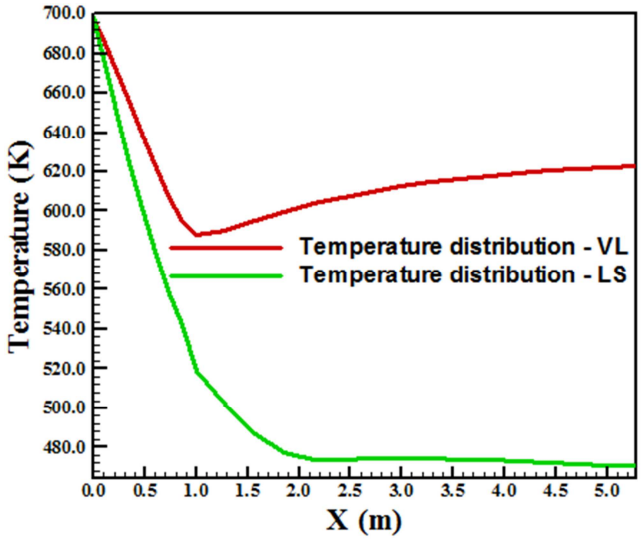

Figure 74. *Wall temperature distributions.*

Figure 74 shows the temperature distributions at wall generated by the [2] and [3] schemes as using the [12] turbulence model in its C-C variant. The [3] temperature distribution is smoother than the [2] one. The [2] temperature distribution decreases and increases along the body, whereas the [3] temperature distribution decreases until reach a constant value. The temperature values at the body end are approximately 620.0 K to the [2] scheme and 470.0 K to the [3] scheme. The maximum temperature value, at the body leading edge, for both solutions is 700.0 K.

5.4. Quantitative Analysis

A possibility to quantitative comparison of the turbulent cases is the determination of the stagnation pressure ahead of the configuration. [27] presents a table of normal shock wave properties in its B Appendix. This table permits the determination of some shock wave properties as function of the freestream Mach number. In front of the blunt body configuration, the shock wave presents a normal shock behavior, which permits the determination of the stagnation pressure, behind the shock wave, from the tables encountered in [27]. So it is possible to determine the ratio pr_0/pr_∞ from [27], where pr_0 is the stagnation pressure in front of the configuration and pr_∞ is the freestream pressure (equals to $1/\gamma$ to the present dimensionless).

Hence, to this problem, $M_\infty = 3.0$ corresponds to $pr_0/pr_\infty = 12.06$ and remembering that $pr_\infty = 0.714$, it is possible to conclude that $pr_0 = 8.61$. Values of the stagnation pressure to the turbulent cases and respective percentage errors are shown in Tab. 3. They are obtained from Figures 3, 4, 11, 12, 19, 20, 27, 28, 35, 36, 43, 44, 51, 52, 59, 60, 67, and 68. As can be observed, the [2] scheme using the [11] turbulence model for all variants has presented the best result, with a percentage error of 0.81%. It is important to observe that, although first order schemes were used, the percentage relative errors were inferior to 7.50%.

Table 3. *Values of the stagnation pressure and respective percentage errors.*

Model:	Scheme - Variant:	pr_0:	Error (%):
[10]	[2]	9.23	7.20
	[3]	8.47	1.63
	[2] – Wilcox	8.68	0.81
	[2] – k-ε	8.68	0.81
	[2] – BSL	8.68	0.81
[11]	[2] – SST	8.68	0.81
	[3] – Wilcox	8.17	5.11
	[3] – k-ε	8.17	5.11
	[3] – BSL	8.17	5.11
	[3] – SST	8.17	5.11
	[2] – LS-LS	8.35	3.02
	[2] – LS-C	8.35	3.02
	[2] – C-LS	8.35	3.02
[12]	[2] – C-C	8.35	3.02
	[3] – LS-LS	8.15	5.34
	[3] – LS-C	8.15	5.34
	[3] – C-LS	8.15	5.34
	[3] – C-C	8.15	5.34

Finally, Table 4 exhibits the computational data of the present simulations. It can be noted that the most efficient is the [2] scheme using the [11] turbulence model in its SST variant. All schemes used a CFL number of 0.10, not necessarily being the maximum CFL number of each one.

Table 4. *Computational data.*

Model:	Scheme – Variant:	CFL:	Iterations:
[10]	[2]	0.10	3,463
	[3]	0.10	3,403
	[2] – Wilcox	0.10	731
	[2] – k-ε	0.10	731
	[2] – BSL	0.10	731
[11]	[2] – SST	0.10	730
	[3] – Wilcox	0.10	2,531
	[3] – k-ε	0.10	2,474
	[3] – BSL	0.10	2,349
	[3] – SST	0.10	2,343
	[2] – LS-LS	0.10	4,845
	[2] – LS-C	0.10	4,849
	[2] – C-LS	0.10	4,845
[12]	[2] – C-C	0.10	4,849
	[3] – LS-LS	0.10	5,748
	[3] – LS-C	0.10	5,747
	[3] – C-LS	0.10	5,747
	[3] – C-C	0.10	5,746

As final conclusion of this study, the [11] turbulence model in its SST variant was the best when comparing these three

turbulence models: [10], [11], and [12]. This choice is based on the best estimative of the stagnation pressure and in the computational efficiency to reach steady state. In a next paper, the present author will study more three different turbulent models to this same problem trying to identify the best of each group and to perform a final analysis to found the best one.

6. Conclusions

In the present work, the [2-3] flux vector splitting schemes are implemented, on a finite-volume context. The three-dimensional Favre-averaged Navier-Stokes equations are solved using an upwind discretization on a structured mesh. The [10] algebraic model, and the [11] and [12] k-ω and $k^{1/2}$-ζ two-equation models, respectively, are used in order to close the problem. The physical problem under study is the supersonic flow around a blunt body configuration. The implemented schemes are first-order accurate in space. The time integration uses a Runge-Kutta method of five stages and is second-order accurate. The algorithms are accelerated to the steady state solution using a spatially variable time step. This technique has proved excellent gains in terms of convergence rate as reported in [13-14].

The results have demonstrated that the [2] scheme using the [11] turbulence model in its SST variant has yielded the best value of the stagnation pressure at the blunt body nose, is the most efficient scheme in the simulations and is the best choice for this study.

Acknowledgment

The author thanks the CAPES by the financial support conceded under the form of a scholarship. He also acknowledges the infrastructure of ITA that allowed the realization of this work.

References

[1] P. Kutler, "Computation of Three-Dimensional, Inviscid Supersonic Flows", *Lecture Notes in Physics*, Vol. 41, 1975, pp. 287-374.

[2] B. Van Leer, "Flux-Vector Splitting for the Euler Equations", *Proceedings of the 8th International Conference on Numerical Methods in Fluid Dynamics*, E. Krause, Editor, *Lecture Notes in Physics*, Vol. 170, 1982, pp. 507-512, Springer-Verlag, Berlin.

[3] M. Liou, and C. J. Steffen Jr., "A New Flux Splitting Scheme", *Journal of Computational Physics*, Vol. 107, 1993, pp. 23-39.

[4] E. S. G. Maciel, "Assessment of Several Turbulence Models Applied to Supersonic Flows in Three-Dimensions – Part I", *Computational and Applied Mathematics*, Vol. 1, No. 4, 2015, pp. 156-173.

[5] E. S. G. Maciel, and N. G. C. R. Fico Jr., "Estudos de Escoamentos Turbulentos Utilizando o Modelo de Baldwin e Lomax e Comparação entre Algoritmos Explícitos e Implícitos", *Proceedings of the III National Congress of Mechanical Engineering (III CONEM)*, Belém, PA, Brazil, 2004. [CD-ROM]

[6] B. S. Baldwin, and H. Lomax, "Thin Layer Approximation and Algebraic Model for Separated Turbulent Flows", *AIAA Paper 78-257*, 1978.

[7] R. W. MacCormack, "The Effect of Viscosity in Hypervelocity Impact Cratering", *AIAA Paper 69-354*, 1969.

[8] T. H. Pulliam, and D. S. Chaussee, "A Diagonal Form of an Implicit Approximate-Factorization Algorithm", *Journal of Computational Physics*, Vol. 39, 1981, pp. 347-363.

[9] A. Jameson, W. Schmidt, and E. Turkel, "Numerical Solution of the Euler Equations by Finite Volume Methods Using Runge-Kutta Time Stepping Schemes", *AIAA Paper 81-1259*, 1981.

[10] P. R. Sparlat, and S. R. Allmaras, "A One-Equation Turbulence Model for Aerodynamic Flows", *AIAA Paper 92-0439*, 1992.

[11] F. R. Menter, and C. L. Rumsey, "Assessment of Two-Equation Turbulence Models for Transonic Flows", *AIAA Paper 94-2343*, 1994.

[12] M. M. Gibson, and A. A. Dafa'Alla, "Two-Equation Model for Turbulent Wall Flow", *AIAA Journal*, Vol. 33, No. 8, 1995, pp. 1514-1518.

[13] E. S. G. Maciel, *Simulations in 2D and 3D Applying Unstructured Algorithms, Euler and Navier-Stokes Equations – Perfect Gas Formulation*. Saarbrücken, Deutschland: Lambert Academic Publishing (LAP), 2015, Ch. 1, pp. 26-47.

[14] E. S. G. Maciel, *Simulations in 2D and 3D Applying Unstructured Algorithms, Euler and Navier-Stokes Equations – Perfect Gas Formulation*. Saarbrücken, Deutschland: Lambert Academic Publishing (LAP), 2015, Ch. 6, pp. 160-181.

[15] R. W. Fox, and A. T. McDonald, *Introdução à Mecânica dos Fluidos*. Ed. Guanabara Koogan, Rio de Janeiro, RJ, Brazil, 632 p, 1988.

[16] E. S. G. Maciel, *Applications of TVD Algorithms in 2D and 3D, Euler and Navier-Stokes Equations in 2D and 3D*. Saarbrücken, Deutschland: Lambert Academic Publishing (LAP), 2015, Ch. 13, pp. 463-466.

[17] D. J. Mavriplis, and A. Jameson, "Multigrid Solution of the Navier-Stokes Equations on Triangular Meshes", *AIAA Journal*, Vol. 28, No. 8, 1990, pp. 1415-1425.

[18] F. R. Menter, "Zonal Two Equation k-ω Turbulence Models for Aerodynamic Flows", *AIAA Paper 93-2906*, 1993.

[19] D. C. Wilcox, "Reassessment of the Scale-Determining Equation for Advanced Turbulence Models", *AIAA Journal*, Vol. 26, No. 11, 1988, pp. 1299-1310.

[20] B. E. Launder, and B. I. Sharma, Application of the Energy-Dissipation Model of Turbulence to the Calculation of Flow Near a Spinning Disc, *Letters in Heat and Mass Transfer*, Vol. 1, No. 2, 1974, pp. 131-138.

[21] K. Y. Chien, "Predictions of Channel and Boundary Layer Flows with a Low-Reynolds-Number Turbulence Model", *AIAA Journal*, Vol. 20, 1982, January, pp. 33-38.

[22] E. S. G. Maciel, "Comparação entre os Modelos de Turbulência de Cebeci e Smith e de Baldwin e Lomax", *Proceedings of the 5th Spring School of Transition and Turbulence (V EPTT)*, Rio de Janeiro, RJ, Brazil, 2006. [CD-ROM]

[23] E. S. G. Maciel, "Estudo de Escoamentos Turbulentos Utilizando os Modelos de Cebeci e Smith e de Baldwin e Lomax e Comparação entre os Algoritmos de MacCormack e de Jameson e Mavriplis", *Proceedings of the 7th Symposium of Computational Mechanics (VII SIMMEC),* Araxá, MG, Brazil, 2006. [CD-ROM]

[24] E. S. G. Maciel, "Assessment of Several Turbulence Models Applied to Supersonic Flows in Three-Dimensions – Part II", Submitted to *Computational and Applied Mathematics* (AASCIT) (under review).

[25] A. Jameson, and D. Mavriplis, "Finite Volume Solution of the Two-Dimensional Euler Equationson a Regular Triangular Mesh", *AIAA Journal*, Vol. 24, No. 4, 1986, pp. 611-618.

[26] E. S. G. Maciel, "Simulação Numérica de Escoamentos Supersônicos e Hipersônicos Utilizando Técnicas de Dinâmica dos Fluidos Computacional", *Doctoral Thesis*, ITA, CTA, São José dos Campos, SP, Brazil, 2002.

[27] J. D. Anderson Jr., *Fundamentals of Aerodynamics*. McGraw-Hill, Inc., EUA, 4th Edition, 1008p, 2005.